Global 30–240 keV proton precipitation in the 17–18 April 2002 geomagnetic storms: 1. Patterns

Xiaohua Fang,[1] Michael W. Liemohn,[1] Janet U. Kozyra,[1] David S. Evans,[2] Anna D. DeJong,[1] and Barbara A. Emery[3]

[1] Global 30–240 keV proton precipitation patterns during the 17–18 April 2002 magnetic storm events were generated using newly developed 3-hour data products of the medium energy proton and electron detector (MEPED) on board the NOAA-15 and -16 satellites. The observational data set was sorted in 1-degree corrected magnetic latitude (CML) and 8-min magnetic local time (MLT) bins. To achieve global coverage, the missing MLT data were filled by interpolation techniques in each 1-degree CML interval. The resulting global 30–240 keV proton precipitation maps, available on a 3-hour cadence, provide new information on the development and variability in the structure of incident high-energy protons on a timescale commensurate with the growth and decay of the plasma sheet and ring current. The change of energetic proton precipitation patterns in the April 2002 storms is quantified in terms of three aspects: hemispheric integrated total particle energy input, midnight proton oval equatorward boundary, and position of proton precipitation peak. In a general sense, as magnetospheric activity intensified, the midnight equatorward boundary tended to move to the lower latitude, while the precipitation peak moved equatorward and westward away from midnight, in agreement with ring current motion. It is well illustrated that energetic proton precipitation patterns can serve as a valuable diagnostic tool for investigating the inner magnetospheric activity.

Citation: Fang, X., M. W. Liemohn, J. U. Kozyra, D. S. Evans, A. D. DeJong, and B. A. Emery (2007), Global 30–240 keV proton precipitation in the 17–18 April 2002 geomagnetic storms: 1. Patterns, *J. Geophys. Res.*, *112*, A05301, doi:10.1029/2006JA011867.

1. Introduction

[2] It has been well-established that the various components of geospace are not isolated but tightly coupled with each other. A direct and visible demonstration of this coupling is the energetic particle injection from the inner magnetosphere to the ionosphere. *Mende et al.* [2002] reviewed four types of processes in the inner magnetosphere that can result in the proton population in the loss cone and ultimately lead to particle precipitation along magnetic field lines into the low-altitude atmosphere. The first way of disturbing the pitch angle distribution is by injecting fresh protons of an isotropic distribution into a region of closed field lines. The second possible mechanism is the pitch angle diffusion due to interaction between electric fields (dc or wave) and particles. Third, proton precipitation can be induced when the region occupied by the particles is compressed by a magnetic reconfiguration. Fourth, in a stretched magnetic field configuration, nonadiabatic particle motions result when the radius of curvature of the stretched magnetic field line is comparable to the gyroradii of energetic ions, leading to violation of the first adiabatic invariant and enhanced ion precipitation. Various approaches have been proposed in the literature for the modeling of proton transport in the Earth's atmosphere [e.g., *Davidson*, 1965; *Jasperse and Basu*, 1982; *Basu et al.*, 1993; *Kozelov*, 1993; *Galand et al.*, 1997; *Solomon*, 2001; *Fang et al.*, 2004, 2005]. Global proton precipitation in conjunction with the transport models provide a valuable way to understand the unique role of protons in magnetosphere-ionosphere-thermosphere coupling. Particle precipitation at low altitudes, in turn, have signatures of magnetospheric activities (which are distant, invisible, and hard to globally measure). The construction of sequential global morphologies of proton ovals, in this sense, offers a powerful remote diagnostic tool for investigating the time evolution of the inner magnetosphere in a global perspective.

[3] Global pictures of proton precipitation have been statistically delineated by *Hardy et al.* [1989], using several years of ion measurements made by Defense Meteorological Satellite Program (DMSP) satellites. Global patterns were derived for protons in the range of 30 eV to 30 keV as

---

[1]Space Physics Research Laboratory, University of Michigan, Ann Arbor, Michigan, USA.
[2]Space Environment Center, National Oceanic and Atmospheric Administration, Boulder, Colorado, USA.
[3]High Altitude Observatory, National Center for Atmospheric Research, Boulder, Colorado, USA.

a function of seven geomagnetic activity levels as defined by Kp. Their findings reveal that the integral proton energy flux has a C-shaped distribution roughly symmetric about a meridian running prenoon to premidnight. The maximum energy flux is found in premidnight, while the minimum in prenoon. A functional representation of the *Hardy et al.* [1989] results was developed to facilitate the use of these average proton precipitation maps [*Hardy et al.*, 1991]. Additionally, *Codrescu et al.* [1997] used a 16-year data set of National Oceanic and Atmospheric Administration (NOAA) Television and Infrared Observation Satellite (TIROS) measurements to construct statistical proton ovals in a higher-energy range of 30–2500 keV. Similarly, they found that energetic proton precipitation had a circular shape with a trough in the prenoon sector.

[4] Statistical analyses are widely used and enrich the understanding of precipitating protons in a global perspective. For example, *Hubert et al.* [2001] assessed auroral Far Ultraviolet (FUV) emissions from global electron and proton precipitations based on the *Hardy et al.* [1987, 1991] empirical models, respectively. The model results showed that proton-dominated N_2 Lyman-Birge-Hopfield (LBH) emissions were located in the afternoon sector with a maximum proton contribution near the equatorward boundary of the statistical electron oval. Statistical methods successfully enrich our understanding of the global morphology of proton precipitation. However, their ability to observe the dynamics of proton ovals is necessarily limited, as statistical maps were built with a large number of data sets constructed from in situ satellite measurements at different times and different locations.

[5] Another approach suitable for global particle precipitation with better time resolution is global imaging. The Imager for Magnetopause-to-Aurora Global Exploration (IMAGE) spacecraft [*Burch*, 2000] is the first and the only satellite with simultaneous global remote sensing of proton ovals. The FUV-SI12 channel [*Mende et al.*, 2000] on board IMAGE had the capability of detecting the Doppler-shifted Lyman α line of hydrogen with a peak sensitivity at slightly longer wavelength of 1218 $\mathring{A}$. Red-shifted Lyman α emissions come from excited downward moving hydrogen atoms, which are generated in an incident proton beam through charge exchange collisions with ambient neutrals. Unlike all previous auroral imagers (such as that on Dynamics Explorer 1 [*Frank and Craven*, 1988] and the POLAR Ultraviolet Imager [*Torr et al.*, 1995]), which cannot discriminate between the proton and electron sources of FUV emissions, IMAGE is able to directly measure proton precipitation on a global scale. IMAGE-FUV global proton images have been used in the analysis of individual precipitation cases [e.g., *Burch et al.*, 2001; *Hubert et al.*, 2004], as well as in the seasonal variation study of statistical patterns [*Coumans et al.*, 2004].

[6] While surpassing the limits of in situ measurements by being able to distinguish temporal and spatial variations, IMAGE is deficient in its lack of information on the spectral characteristics. The *Hardy et al.* [1989, 1991] empirical model has to be implemented to approximate the mean energy of precipitating protons [*Coumans et al.*, 2004]. Proton energy fluxes can then be inferred from SI12 images using the Ly-α efficiency function [*Gérard et al.*, 2001]. In contrast to the inherent limitation of IMAGE with respect to

the spectral characteristics, in situ space-borne measurements are valuable in offering particle compositions and energy spectra and cannot be replaced at present. This study aims to achieve a balance in the present situation between temporal-spatial resolution and spectral-compositional information.

[7] In this paper, global coverage of energetic proton precipitation at a 3-hour cadence is yielded through the integration of in situ NOAA satellite measurements. Global 30–240 keV proton precipitation patterns are constructed during a specific geomagnetic storm period: 17–18 April 2002. The understanding of proton oval dynamics will be placed in the context of the interaction between the solar wind and the Earth's inner magnetosphere.

2. April 2002 Geomagnetic Storm Events

[8] The geomagnetic storm events of April 2002 offer a great opportunity to observe how the Earth's geospace system responds to violent disturbances occurring on the Sun. In the month of April 2002, the solar active region 9906 underwent three eruptions as it traversed the solar disk: two of them produced halo coronal mass ejections (CMEs), and the third produced an X-1 class solar flare accompanied by a CME, which was not directed at the Earth. As the first interplanetary CME (ICME) impacted the Earth's magnetosphere at ∼1107 UT on 17 April, a double-peaked magnetic storm was triggered. The shock and the sheath preceding the ICME drove the first peak while the second one was due to the passage of the magnetic cloud itself. Before the first storm fully subsided, the second ICME struck the Earth at ∼0835 UT on 19 April and drove a second storm with a similar double-peaked structure. On 23 April at ∼0448 UT, a third storm occurred in association with the solar flare eruption. Since the third ICME was not directly aimed at the Earth, the disturbances of the magnetosphere were at weak activity levels. The present study focuses on the global energetic proton precipitation patterns during the 17–18 April period. This study explores and compares the inner magnetospheric activity in response to three different solar wind drivers: (1) ambient (prestorm) conditions, (2) compressed sheath region associated with high dynamic pressure and highly fluctuating interplanetary magnetic field (IMF), and (3) magnetic cloud itself associated with low solar wind density and rather smoothly varying IMF.

[9] Figure 1 shows an overview of the solar wind parameters and geophysical responses in a 3 day interval of 16–18 April 2002. The solar wind density and speed are from the Solar Wind Electron Proton and Alpha Monitor [*McComas et al.*, 1998] onboard the Advanced Composition Explorer (ACE) satellite. The z-component of IMF in geocentric solar magnetospheric (GSM) coordinates are from ACE Magnetic Field Experiment [*Smith et al.*, 1998]. Note that a 46-min time shift has been implemented to allow for the solar wind propagation delay from the x-GSM location of the ACE satellite (∼223 Re) to the Earth's magnetopause (∼10 Re). Figure 1d presents the calculated solar wind motional electric field, $E_y = -V_{sw} \times B_z$, which is proportional to the solar wind energy input to the Earth due to the magnetic field merging at the dayside magnetopause
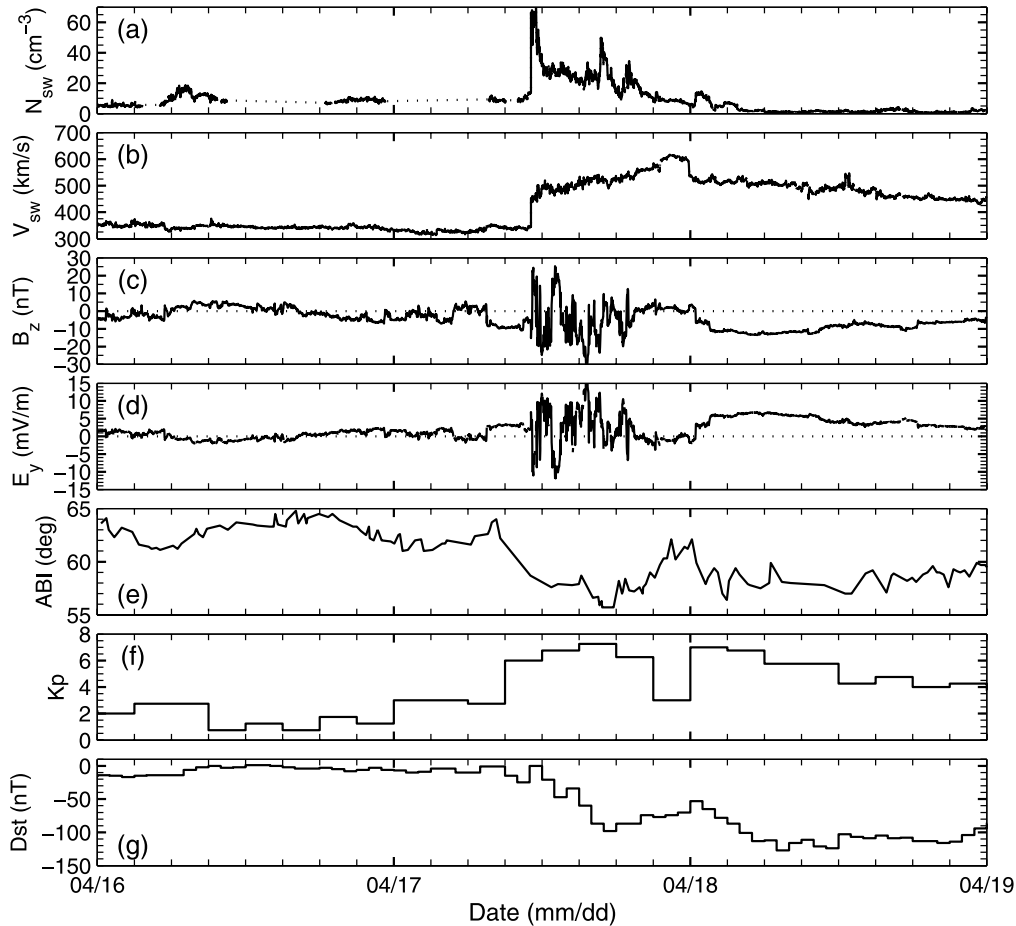
Figure 1. Solar wind and geophysical conditions during the period of 16 April to 18 April 2002: (a) solar wind density; (b) solar wind velocity $V_{x,GSM}$; (c) interplanetary magnetic field $B_{z,GSM}$; (d) solar wind motional electric field; (e) ABI index; (f) Kp index; and (g) Dst index.

[*Burton et al.*, 1975], and is correlated with the magnetospheric convection [*Reiff et al.*, 1981].

[10] Figure 1e is the Air Force Research Laboratory midnight auroral boundary index (ABI) [*Gussenhoven et al.*, 1983; *Madden and Gussenhoven*, 1990]. The equatorward auroral boundary in corrected magnetic latitude (CML) is determined from in situ energetic electron precipitation measurements on board the DMSP satellites and then scaled to the midnight sector using a linear statistical relationship that is established in 1-hour magnetic local time (MLT) bins between the equatorward boundary and Kp.

[11] To illustrate the level of geomagnetic activity, presented in Figures 1f and 1g are the Kp and Dst indices in April 2002. Kp is used as a global magnetic activity indicator and often has significant contribution from the high-latitude auroral electrojets. The Dst index aims to represent the strength of the ring current and thus has been adopted as a proxy for magnetic storm severity and geoeffectiveness of solar wind structures. In Figure 1 the double-peaked feature of the storm is clearly related to the geophysical conditions. The abrupt enhancements of the solar wind density and velocity at ~1107 UT on 17 April (Figures 1a and 1b) indicate the arrival of a solar wind dynamic pressure impulse or an interplanetary shock associated with the first ICME. As a consequence of the large fluctuating IMF B_z in the

magnetic cloud sheath region (Figure 1c), the storm developed and reached the first minimum in Dst of −98 nT at 1800 UT on 17 April. Correspondingly, Kp reached a maximum of 7+ and ABI was at the very low level of 55.6°. The magnetic cloud itself arrived at the Earth on 18 April with the clear signature of low solar wind density and stable southward IMF. As a result, the storm main phase intensified and reached the minimum value of $Dst = $ −127 nT at 0800 UT on 18 April. During the rest of that day, the geomagnetic activity remained at quite disturbed levels: Dst less than −100 nT, Kp hovering around 4, and ABI well below 60° latitude.

[12] One prominent feature of the selected geomagnetic storms is the global sawtooth oscillations associated with the magnetic cloud passage during 18 April 2002: quasi-periodic, nearly dispersionless injections of energetic particles observed at geosynchronous orbit [*Henderson et al.*, 2006; *Clauer et al.*, 2006; *Liemohn et al.*, 2007]. Sawtooth oscillations are clear in the variation of high-energy particle intensities observed at geosynchronous orbit by the synchronous orbit particle analyzer [*Belian et al.*, 1992] on board the Los Alamos National Laboratory spacecraft: sharp increases followed by gradual flux dropouts. The processes are repeated roughly every 2–3 hours. Unlike isolated substorms, in which particle injections usually take place only in the near-midnight sector, the sawtooth signature in

Table 1. Characteristic Energies of the MEPED Solid State Directional Detectors

	Energy Range, keV	
Channel	Protons	Electrons
1	30–80	>30
2	80–240	>100
3	240–800	>300
4	800–2500	
5	2500–6900	
6	>6900	

particle intensities were observed almost simultaneously at all energies by the geosynchronous satellites in a broad range of magnetic local times. In consideration of the characteristics usually associated with isolated substorms (that is, magnetic field dipolarization and stretching in the tail region, energetic plasma sheet particle injections, auroral onsets), sawtooth events were suggested as a sequence of substorm injections [*Reeves et al.*, 2002; *Huang et al.*, 2003; *Henderson*, 2004; *Lui et al.*, 2004]. However, there are debates going on about whether sawtooth oscillations are due to periodic substorms or driven by solar wind dynamic pressure enhancements [*Lee et al.*, 2004; *Huang et al.*, 2005]. *Liemohn et al.* [2007] employed the ring current-atmosphere interaction model (RAM) [*Fok et al.*, 1993; *Jordanova et al.*, 1996; *Liemohn et al.*, 1999, 2004] to simulate the inner magnetospheric responses by comparing against *Dst** and energetic neutral atom images of hot ions. The modeling results implied that the inner magnetospheric reconfigurations in association with the global sawtooth oscillations on 18 April were quite different from those associated with a sheath region on 17 April. The storm-substorm related issues are beyond the scope of this paper and not discussed. Rather, this study concentrates on the energetic proton precipitation patterns, and uses them as a diagnostic tool to investigate the inner magnetospheric activities in the storm events.

3. Instrumentation

[13] A newly developed data product is proposed for use in the current study: global maps of the ion precipitation from NOAA Polar Orbiting Environmental Satellites (POES) measurements. The POES series satellites circle the Earth from pole to pole in Sun-synchronous polar orbits at around 850 km altitude. With an inclination of around 98°, the asymmetric gravitational pull of the Earth introduces a slow precession in the orbital planes so that the satellites pass the equator at approximately the same geographic local time each orbit. By this means, the Sun-synchronous polar track provides daily global coverage for a single satellite. Another advantage is that their suborbital tracks do not repeat on a daily basis, given the fact that the number of orbits per day is not an integer. During the interval of interest (April 2002 storm events), NOAA-15 and -16 were the only POES satellites in operation and therefore were chosen here to provide a global-scale inventory of injecting high-energy protons. These two satellites have orbits roughly perpendicular to each other. NOAA-15 passes over the local evening/morning sector with northbound equatorial crossings at ~1930 local time (LT) while

NOAA-16 is over the early afternoon/postmidnight sector ascending at ~1400 LT.

[14] The Space Environment Monitor (SEM) on board the NOAA/POES satellites is a multichannel charged-particle spectrometer which senses particles over a broad range of energies. The SEM consists of two instruments: the total energy detector (TED) and the medium energy proton and electron detector (MEPED). The TED measures electron and proton energy fluxes in the 0.05 to 20 keV energy range. The MEPED measures higher energy particles and provides both directional and omnidirectional measurements. Directional measurements are made by two solid state detector telescopes. One is oriented to view outwards along the Earth-satellite radial vector, and the other is oriented to view about 90° to the first. Each telescope has a 30° field of view. The nominal energy intervals measured by the MEPED directional detectors are summarized in Table 1 for both protons and electrons. The MEPED also includes omnidirectional solid state sensors providing measurements of relativistic protons at energies of >16 MeV, >35 MeV, >70 MeV, and >140 MeV. In this study we use only proton data collected by the MEPED directional telescopes (see *Evans and Greer* [2000] for more details of the MEPED instrument). Note that no ion mass separation is provided in the SEM. In this study, it is assumed that all the MEPED responses to ion impact are from protons.

4. Data Analysis Procedures

[15] In this section the key analysis procedures are presented for the NOAA/POES proton data from the MEPED instruments. The data fitting methods will be described for the construction of global energetic proton precipitation patterns by interpolating the data in local time.

4.1. NOAA/POES Data

[16] In correspondence with the objective of providing an inventory of the energetic proton input to the Earth's atmosphere, only data from the zenith viewing detectors are used in the current analysis. The orbital period of the NOAA/POES satellites is about 102 min, so in any 3-hour interval NOAA-15 and NOAA-16 will totally make between six and eight transits over the northern polar region. After including the observations that were made in the southern hemisphere (we will come back to this later in section 4.2), there will be more than 12 samples at a given latitude in the northern hemisphere. Considering that the two satellites are in nearly perpendicular polar orbits, this number of data points is regarded as the minimum needed to generate a believable global specification. Thus the time cadence adopted for the global maps is 3 hours. The center times of these intervals for each day are 0000, 0300, 0600, 0900, 1200, 1500, 1800 and 2100 universal time (UT). The 16-s averaged NOAA energetic particle data are extracted for the interval 1.5 hours before and after each UT center time. Keep in mind that in the construction of a snapshot on a 3-hour cadence, it is presumed that there is no severe fluctuation in particle injection during this time interval. While this cadence is not sufficient to resolve rapid precipitation variations, it is the best rate possible with NOAA's present fleet of satellites, and it is fast enough to resolve large-scale changes in the precipitation within each phase of a storm.

(a) North

April 17, 2002
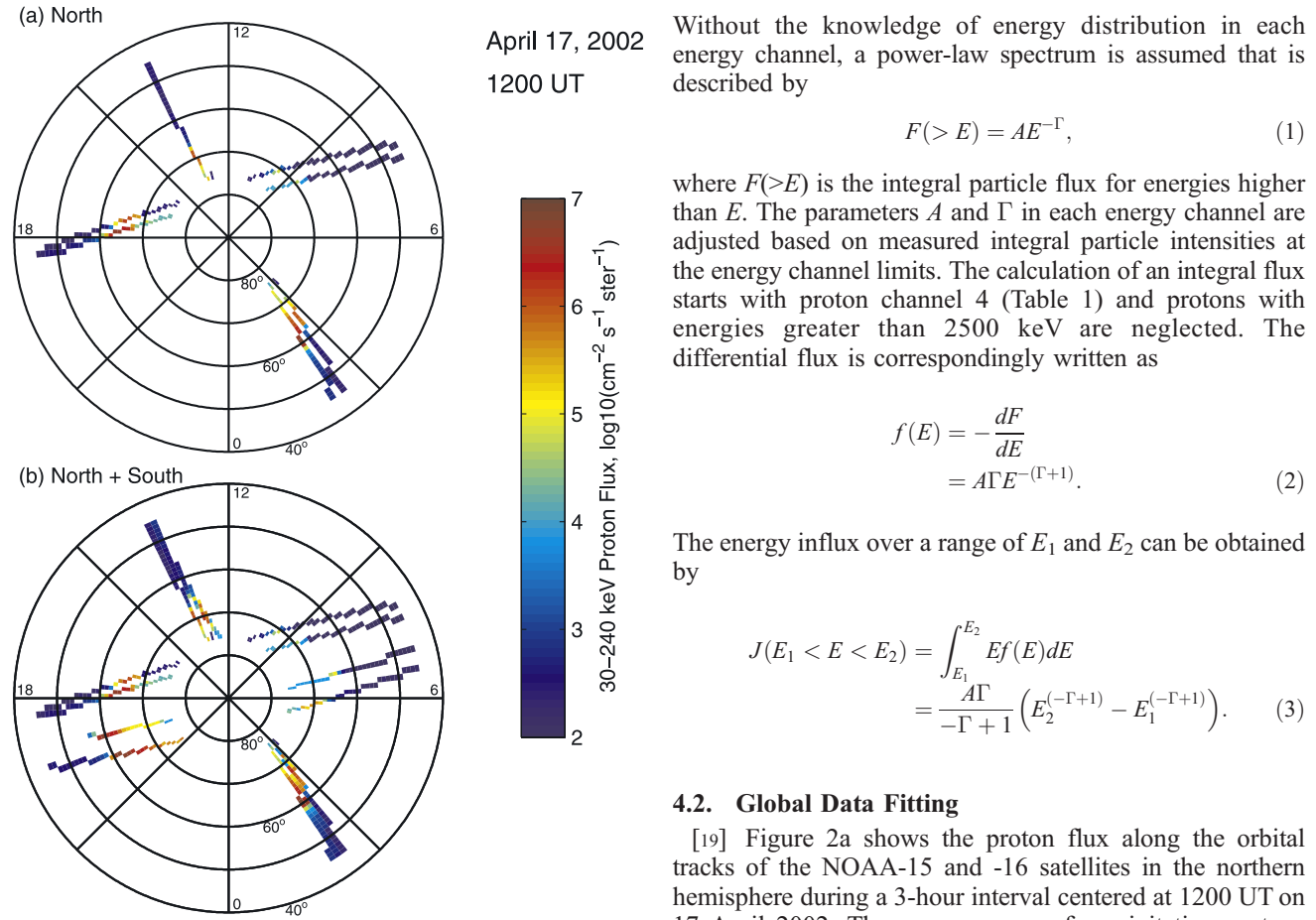
1200 UT

Figure 2. The 30–240 keV proton flux along the orbital tracks of the NOAA-15 and -16 satellites during a 3-hour interval centered at 1200 UT on 17 April 2002. The view is over the north pole in CML-MLT coordinates with local noon to the top. The perimeter latitude is 40° north and the solid circles are 10° apart. The data represent the proton injection (a) observed in the northern hemisphere and (b) merging observations made in the southern hemisphere with those in the northern hemisphere.

Without the knowledge of energy distribution in each energy channel, a power-law spectrum is assumed that is described by

$$F(> E) = AE^{-\Gamma}, \qquad (1)$$

where $F(>E)$ is the integral particle flux for energies higher than E. The parameters A and Γ in each energy channel are adjusted based on measured integral particle intensities at the energy channel limits. The calculation of an integral flux starts with proton channel 4 (Table 1) and protons with energies greater than 2500 keV are neglected. The differential flux is correspondingly written as

$$
\begin{aligned}
f(E) &= -\frac{dF}{dE} \\
&= A\Gamma E^{-(\Gamma+1)}.
\end{aligned} \qquad (2)
$$

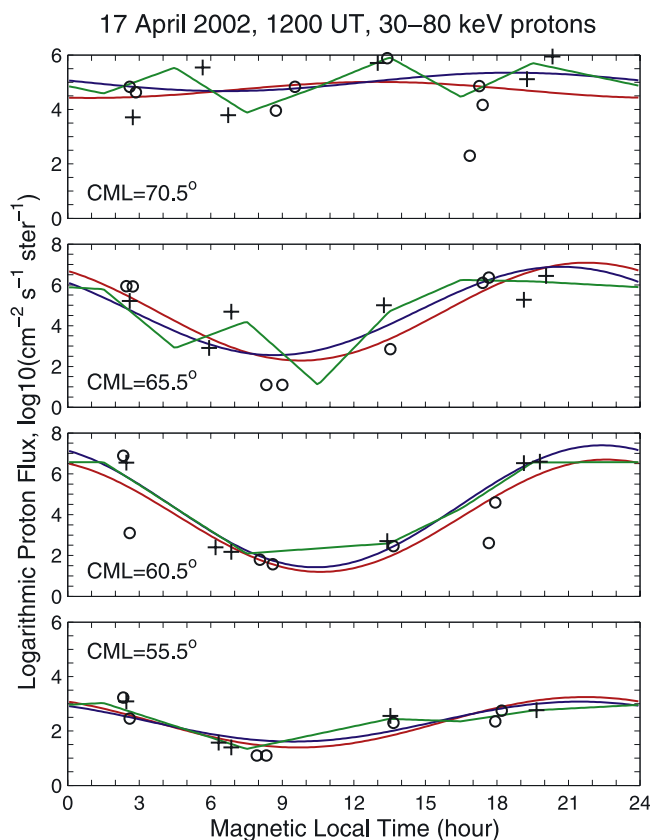The energy influx over a range of E_1 and E_2 can be obtained by

$$
\begin{aligned}
J(E_1 < E < E_2) &= \int_{E_1}^{E_2} E f(E) dE \\
&= \frac{A\Gamma}{-\Gamma+1}\left(E_2^{(-\Gamma+1)} - E_1^{(-\Gamma+1)}\right).
\end{aligned} \qquad (3)
$$

4.2. Global Data Fitting

[19] Figure 2a shows the proton flux along the orbital tracks of the NOAA-15 and -16 satellites in the northern hemisphere during a 3-hour interval centered at 1200 UT on 17 April 2002. The energy range of precipitating protons considered in this study is 30–240 keV. The chosen energy range is enough to be representative of the majority of the ring current energy content, while a lower energy range is dominated by plasma sheet precipitation. Note that in the derivation of the proton energy influx within 30–240 keV (equation 3), the particles in channels 3–4 (Table 1) are taken into account for the integral number flux calculation. To increase the number of data points available for fitting, data taken over the southern hemisphere in a given CML-MLT pixel were directly transferred to the northern hemisphere whenever there was no entry at the magnetic conjugate point. The proton intensity after this transformation over Figure 2a is illustrated in Figure 2b.

[20] It is important to note that by directly mapping southern hemispheric observations to fill the empty entries at magnetic conjugate points in the northern hemisphere, we assume a north-south symmetry in proton precipitation during 17–18 April 2002. This is consistent with the isotropic assumption we have made in the particle pitch angle distribution. However, an uncertainty is associated with this simplified assumption, whose validity is hard to be evaluated. This is because there are rare simultaneous observations at magnetic conjugate points to verify the scheme we have used to increase the density of data points used for making a fit over MLT at a given CML. The nature of the NOAA-15 and NOAA-16 satellite orbits simply prevents simultaneous conjugate measurements from happening.

[21] However, there is an indirect support to this assumption coming from the statistical study of lower-energy

[17] The 3-hour proton data are then binned into corrected magnetic latitude and magnetic local time based upon a magnetic field model that is independent of magnetic disturbance level [*Raben et al.*, 1995]. The grid consists of 180 MLT bins, each 8-min wide, and 31 CML bins, with 1° spacing covering the range of 45° to 76°. Data are extracted only for L-values greater than 2.0, or CML >45°, under the assumption that particle precipitation at lower latitudes would not contribute significantly to the global energy budget. The fluxes at lower latitudes are nearly negligible. Because of the Sun-synchronous, ~98° orbital inclination of the NOAA/POES satellites, during portions of the UT day the satellites do not reach CMLs much above 76°. For the current purpose of analyzing ring current proton precipitation, however, an upper limit of CML = 76° is enough.

[18] Over a 1-degree CML by 8-min MLT pixel, an isotropic flux distribution is assumed in particle injection.

17 April 2002, 1200 UT, 30–80 keV protons

Figure 3. Interpolated 30–80 keV proton fluxes at four 1-degree CML bins every 5° from (top) CML = 70.5° to (bottom) CML = 55.5°, as marked. The interpolations are carried out for the particle data in a 3-hour interval centered at 1200 UT on 17 April 2002. Open circles represent observations made in the northern hemisphere while pluses represent additional data points after the interhemispheric data transfer from the southern hemisphere. Red, blue, and green curves show the results of data fitting to the total data (open circles and pluses) by cosine fit to data points, cosine fit to MLT bin averages, and linear fit to MLT bin averages, respectively.

(<20 keV) ion precipitation by B. A. Emery et al. (Seasonal and *Kp* variations in the auroral electron and ion hemispheric power after intersatellite adjustments, submitted to *J. Geophys. Res.*, 2007, hereinafter referred to as Emery et al., submitted manuscript, 2007). They used a 8-year data set of NOAA SEM-2 <20 keV electron and ion measurements to estimate the electron and the total (electron and ion) hemispheric powers, that is, hemispheric integrated precipitating particle energy fluxes. The ion hemispheric power is thus estimated by subtracting the electron hemispheric power from the total value. In their statistical study, the data were sorted in the better sampled southern hemisphere as a function of season and *Kp*. The selected April 2002 storms in the present paper correspond to a southern hemisphere fall season with high solar flux values ($F_{10.7} > 150$). If we assume that northern hemisphere data in April 2002 (spring) is reasonably analogous to southern hemisphere spring data (because solar illumination and therefore ionospheric conductances should be the same),

then we can use Emery et al.'s southern hemisphere results for this discussion. It is shown by Emery et al. (submitted manuscript, 2007) that the hemispheric integrated <20 keV proton energy inputs during the southern hemisphere fall and spring seasons have very close values (case for high solar flux in Table 3, Emery et al., submitted manuscript, 2007). The fall to spring ratios of the ion hemispheric powers for *Kp* lower than 7+ lie within a range of 0.95–1.3, with a mean of 1.02. It should be noted that symmetry for the low energy data does not necessarily imply symmetry at the higher energies. However, given the close symmetry between fall and spring seasons for <20 keV ion energy inputs in the southern hemisphere, a north-south symmetry assumption is therefore made for 30–240 keV proton precipitation in this study.

[22] The net result of the initial data processing was the creation of a comprehensive data set of differential proton fluxes within MEPED energy channels 1–4 (Table 1). Observations in the southern hemisphere were transferred into the magnetic conjugate point whenever there was no north entry. The data set was sorted in 1-degree CML and 8-min MLT bins. An example is presented in Figure 2b. This is the data used to fit for global coverage.

[23] To achieve global coverage, the missing MLT data were filled by interpolation techniques in each 1-degree CML bin. The interpolation procedures were separately implemented for each proton energy channel in a logarithmic (base 10) scale. Four approaches were carried out and compared: cosine or linear fits to the data points themselves and these same fits to the MLT bin averages instead. By cosine fitting, it is meant that a 3-parameter cosine function was used in the least squares sense. The differential particle flux at any MLT (in hour) is written as

$$f(\text{MLT}) = a \, \cos(\omega(\text{MLT} + b)) + c, \qquad (4)$$

where $\omega = 2\pi/24$ allows for the 24-hour periodicity in MLT. The three unknowns, a, b, and c were determined using the least squares approximation. In addition to interpolating over individual data points, interpolations were also performed of MLT bin averages. The differential proton flux was first grouped into 8 MLT bins, that is, 0–3, 3–6,..., and 21–24 hours. The logarithmic values of the averaged particle intensities in these bins were then used to carry out interpolations using the cosine or linear fit. Comparing the fits to the 8-min MLT binned data points and the 3-hour MLT bin averages allows for an assessment of the sensitivity of the patterns to data resolution.

[24] Figure 3 shows the interpolation results of 30–80 keV protons in a 3-hour interval centered at 1200 UT on 17 April 2002. As an example, the interpolations were compared at four selected 1-degree CML bins spaced 5° apart. Note that the linear interpolations between data points simply correspond to the line segments connecting adjacent symbols (open circles and pluses) in Figure 3, and thus not shown here to make the plots easier to view. The derived precipitating 30–80 keV proton patterns in the CML range of 45°–75° are presented in Figure 4, which displays the four spatial interpolations. The same procedures are applied to the protons in the energy channel of 80–240 keV, and the fitting results are displayed in Figures 5 and 6.
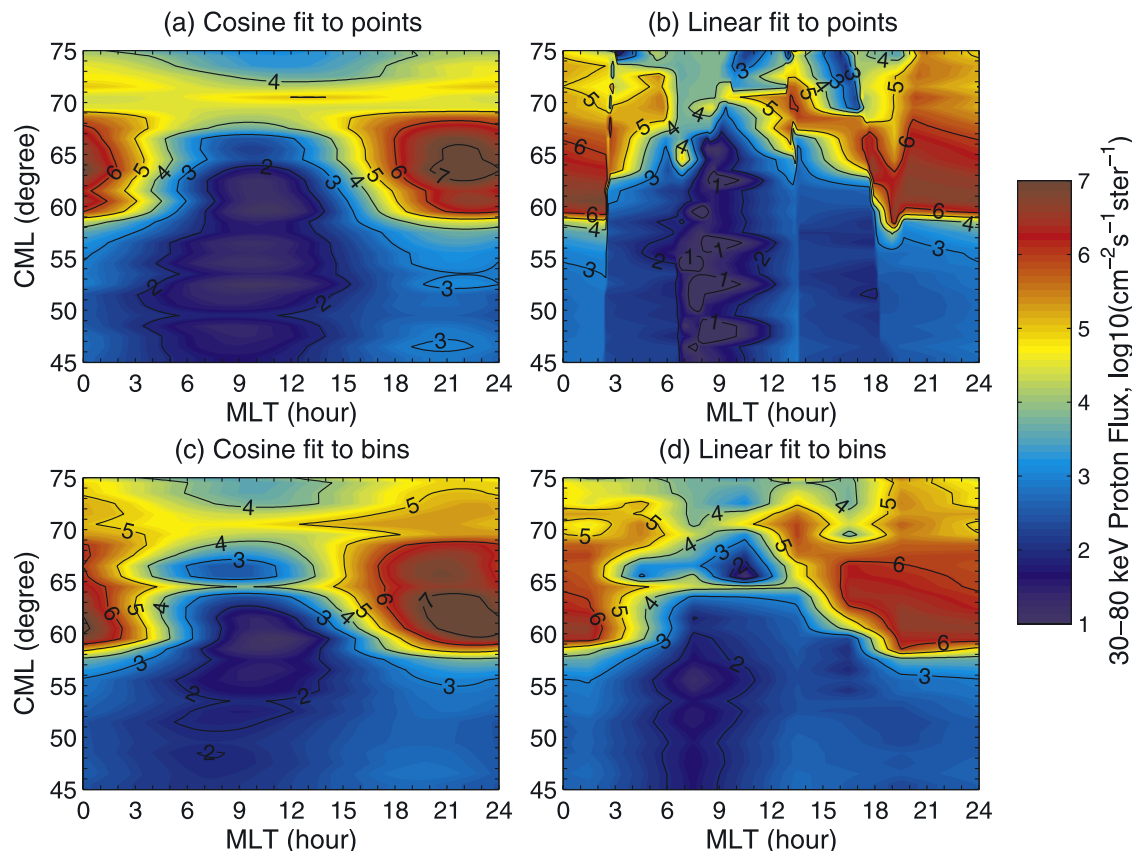
Figure 4. Interpolated 30–80 keV proton precipitation patterns for 17 April 2002, 1200 UT. Four spatial interpolation methods were used: (a) cosine fit to data points, (b) linear fit to data points, (c) cosine fit to MLT bin averages, and (d) linear fit to MLT bin averages.

[25] It is clearly demonstrated in Figures 3 to 6 that the linear fits introduce abrupt jumps in particle intensities, which are nonphysical and thus not acceptable. However, without any specialized knowledge, it is hard to decide which of the cosine interpolations is in better accordance with the MLT dependence of high-energy proton precipitation. It has been shown that the cosine fits to either data points or MLT bin averages generate very similar global distributions. Although some differences exist in regional small-scale features sensitive to the interpolation approaches, this study is more interested in observing precipitating high-energy protons at the top of the atmosphere on a planetary scale and putting the understanding of particle injection in the context of magnetospheric activities. The regional difference due to different fitting methods is thus not so important in this sense. Furthermore, given that observational data points in each 1-degree CML bin are not evenly spaced in MLT (see Figures 2, 3, and 5), the approach of cosine fitting to data points inevitably results in more weights being placed on some MLTs and less on others. By MLT bin averaging, however, such a disadvantage can be avoided. Additionally, a cubic spline fitting method has been tested and left out of consideration because of resulting unreasonable fluctuations in MLT. In this work, the missing MLT data in each 1-degree CML bin is filled in by applying a cosine fit to the 3-hour MLT bin averaged data, and

generating global 30–240 keV proton precipitation patterns throughout the April 2002 storms.

5. The 30–240 keV Proton Precipitation Patterns

5.1. General Description

[26] Figures 7 and 8 present number fluxes and integrated energy fluxes for precipitating 30–240 keV protons during the April 2002 storm events. The patterns are displayed in dial plot format versus CML and MLT, with a view looking down from over the North Pole. Remember that there is no data at latitudes higher than 76°. Note that in Figure 8, the energy flux unit of 1 keV cm^{-2} s^{-1} $ster^{-1}$ is equivalent to 5×10^{-9} erg cm^{-2} s^{-1} under the assumption of an isotropic proton flux distribution.

[27] As seen in Figures 7 and 8, the patterns of the number flux and energy flux are similar in global morphologies. The proton precipitation maps can be generally characterized by a C-shaped morphology with a roughly symmetric distribution about a meridian running premidnight to prenoon with a trough in the dawn-noon quadrant. The specific position of the oval can change significantly in the storm events and will be discussed with regard to the relationships with geomagnetic indices presented below in section 5.5. The general C-shaped morphology is qualitatively consistent with the expectations from the statistical
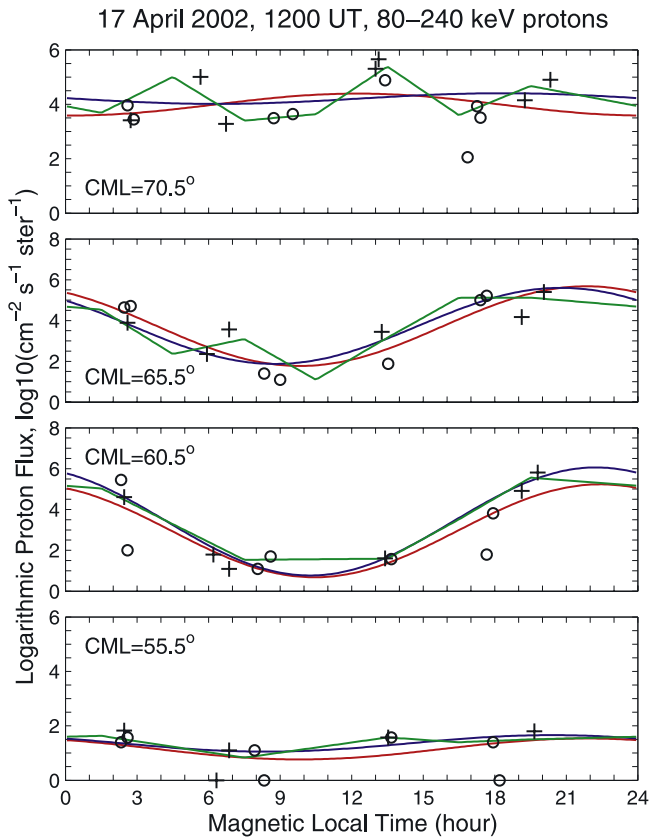
Figure 5. Similar to Figure 3, but for 80–240 keV protons.

studies of *Hardy et al.* [1989] and *Codrescu et al.* [1997]. It is worth noting that, however, the maxima of proton number fluxes are located in the premidnight sector, rather than centered in the dayside cusp region as demonstrated by *Hardy et al.* [1989]. This can be explained by observing that in Figures 3 and 5 (top), there is an underestimation of the number flux by the cosine fitting at very high latitudes (CML >70°) around noon. However, precipitating protons in the cusp region carry much lower energy flux [*Hardy et al.*, 1989]. In fact, the peak of the energy flux occurs mainly premidnight at magnetic latitudes lower than 70°, as shown in Figure 8.

[28] As a global and dynamic phenomenon at the footprint of the inner magnetosphere, particle precipitation provides a unique opportunity to explore how the Earth's geospace system reacts to the solar wind energy input. What is seen in the sequence of dial plots in Figures 7 and 8 should be placed in the context of solar wind driving.

5.2. Prestorm Precipitation Patterns

[29] The first plots in Figures 7 and 8 show a quiet period (16 April, 1200 UT) prior to the arrival of the interplanetary shock on 17 April, typified by intervals of very weak and slightly positive IMF B_z and low dynamic pressure. In this quiet time, weak plasma sheet ion precipitation was observed on the nightside between the magnetic latitudes of 65° and 70°. The energy influx peak was ~0.005 erg cm^{-2} s^{-1}. The next three plots in Figures 7 and 8 (17 April, 0300–0900 UT) show the proton precipitation just prior to the initiation of the magnetic storm. The nightside auroral oval considerably

expanded and covered a larger region with the peak energy flux increasing by one order of magnitude to more than 0.05 erg cm^{-2} s^{-1}. The solar wind data in Figure 1 shows that there was a more than 1-hour period of B_z <−5 nT (17 April, 0330–0441 UT) and a nearly 3-hour period of more negative B_z (<−8 nT, between 17 April, 0735 UT and 1030 UT). The resulting motional electric field E_y considerably enhanced magnetospheric convection and thus the pressure buildup in the plasma sheet, leading to more proton precipitation on the nightside.
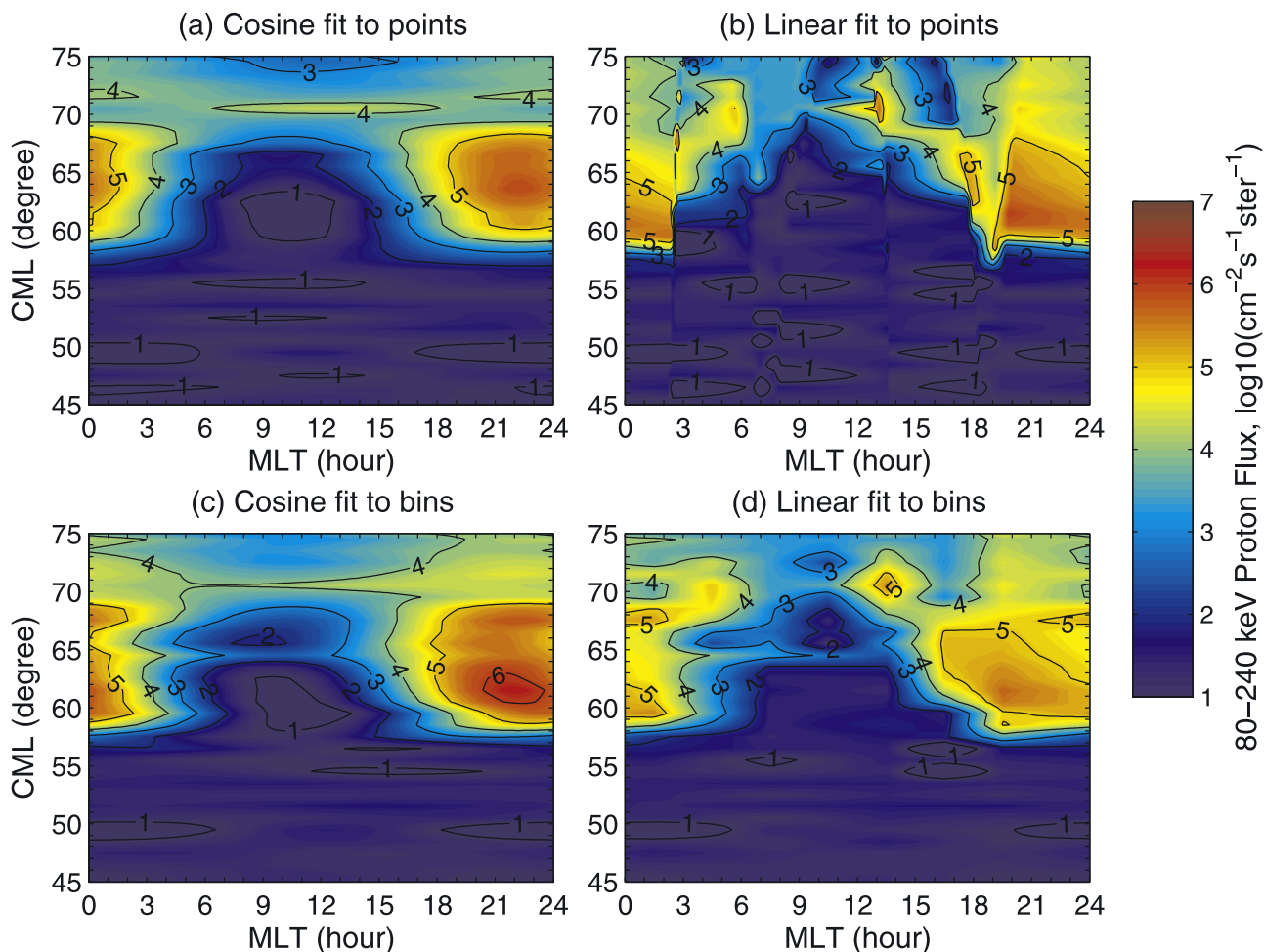
5.3. Sheath Driven Storm Patterns

[30] On 17 April 2002 at 1107 UT, a magnetic storm was triggered by the arrival of a strong interplanetary shock together with largely fluctuating IMF preceding the ICME. The solar wind conditions in Figure 1 shows that highly variable and strong B_z (<−20 nT) was embedded within the sheath, creating a large E_y (>10 mV m^{-1}) and a large energy input. A high pressure impulse associated with the magnetic cloud driven shock significantly compressed the magnetosphere, which can be as geoeffective as strong southward IMF [*Siscoe et al.*, 2002]. The high solar wind dynamic pressure and southward IMF B_z fluctuations lasted from 1107 UT until ~2100 UT after which the dynamic pressure decreased markedly and the IMF B_z relaxed towards zero.

[31] A prominent feature during the interval around 1107–2100 UT is a quick global magnetospheric response to solar wind dynamic pressure enhancement. High solar wind dynamic pressure and strong southward IMF B_z expanded, thickened, and intensified the auroral oval precipitation at all MLTs almost instantaneously (referring to the second rows of Figures 7 and 8). On the dayside, considerable proton precipitation occurred at CML >70° at the first beginning of the sheath driven storm (see the first plots in the second rows of Figures 7 and 8). In the following 6 hours, dayside proton precipitation developed as the equatorward edge of the proton oval (defined here as an energy flux larger than 0.005 erg cm^{-2} s^{-1}) moved to lower latitudes by nearly 10° to about CML = 60° in the morning sector. Auroral intensification at all local times in response to the solar wind dynamic pressure pulse is consistent with the results of *Chua et al.* [2001] and *Lyons* [2000].

[32] Superposed on these plots are strong duskside precipitation peaks from the ring current. The large enhancement in proton precipitation, mostly in the dusk-midnight quadrant, resulted from an intensified partial ring current in the storm main phase [cf., *Liemohn et al.*, 2001a, and references therein]. For example, during the 3-hour interval centered at 1200 UT on 17 April, the precipitating number flux and energy flux increased by one order of magnitude almost everywhere, with a peak in the fit of 2.9×10^7 cm^{-2} s^{-1} ster^{-1} and 6.6 erg cm^{-2} s^{-1}, respectively, at 61.5° CML and 2156 MLT. A minimum in *Dst* occurs on 17 April at 1800 UT which is reflected in a strong duskside precipitation. The duskside ring current population weakened during the northward IMF interval from 17 April, 1930 UT to 18 April, 0000 UT. As a consequence, particle precipitation into the ionosphere distributed relatively evenly on a global scale while the intensity was significantly depleted (the last plot in the second rows of Figures 7 and 8).

Figure 6. Similar to Figure 4, but for 80–240 keV protons.

5.4. Magnetic Cloud Driven Storm Patterns

[33] Beginning after 0000 UT on 18 April 2002, the magnetic cloud itself reached the Earth. The IMF turned sharply and remained steadily southward $B_z < -10$ nT for >18 hours (see Figure 1). This longer period of southward B_z was correlated with the development of a second main phase of the storm, which had a minimum *Dst* of -127 nT at 0800 UT on 18 April and sustained *Dst* <-100 nT in the next 10 hours. Enhanced magnetospheric convection was produced by intervals of prolonged southward IMF. A ring current was therefore rebuilt, resulting in again significant proton precipitation to the ionosphere, as seen in the bottom two rows of Figures 7 and 8. A noteworthy phenomenon during 18 April 2002 is the sawtooth oscillations of >50 keV proton injection observed at the geosynchronous satellites. The recently discovered phenomenon of sawtooth oscillations in the inner magnetosphere are characterized by quasi-periodic (usually 2–3 hours) energetic particle injections observed in a broader local time range, from midnight to well past the terminators [*Reeves et al.*, 2003; *Henderson*, 2004]. However, the understanding of what drives sawtooth-like profiles in particle flux time series is just beginning and still far from adequate [e.g., *Henderson*

et al., 2006; *Clauer et al.*, 2006; *Liemohn et al.*, 2007]. This study does not attempt to explain the mechanism of sawtooth events, which is well beyond the scope of this work, rather this endeavor is focused on energetic proton precipitation patterns. As clearly demonstrated in Figures 7 and 8, significant proton precipitation extended over all local times. The regions of the energy flux larger than 0.05 erg cm^{-2} s^{-1} spanned almost three quadrants, from noon to dawn through the evening sector.

[34] As shown in Figures 1, 7, and 8, global proton precipitation morphologies and intensities were strongly correlated with the plasma sheet and ring current activities in the storm evolution. Evidently different precipitation patterns were followed during the sheath driven and the magnetic cloud driven storms. Because of the high solar wind dynamic pressure together with intervals of southward IMF B_z, the sheath driven storm on 17 April led to more plasma sheet pressure buildup and thus higher auroral activity than the magnetic cloud driven storm with sawtooth oscillations on 18 April. Therefore global energetic proton precipitation provides a valuable diagnostic tool for investigating the inner magnetospheric activity in response to solar wind drivers.
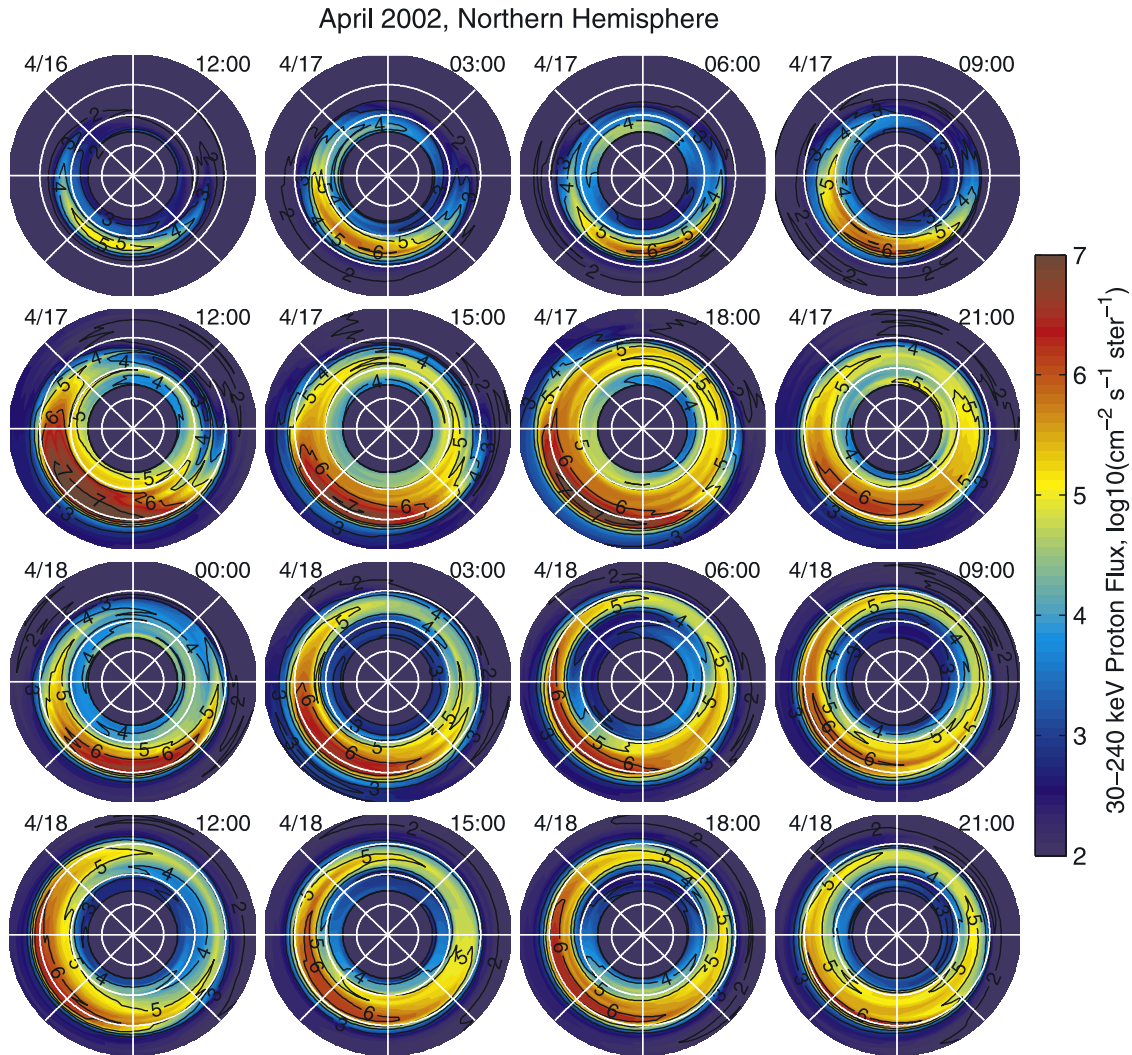
Figure 7. Global patterns of precipitating $30-240$ keV proton number fluxes in the April 2002 magnetic storm events. The patterns are displayed in CML-MLT coordinates, with local noon (1200 MLT) to the top and dawn (0600 MLT) to the right. The perimeter latitude is $50°$ north and the white circles are $10°$ apart. Time tags indicate the center time of each 3-hour time interval. The day of April 2002 is shown in the upper left and the universal time is shown in the upper right of each pattern. The first pattern is for 1200 UT on April 16. The rest shows the patterns on a 3-hour cadence, starting from 0300 UT on April 17 and ending at 2100 UT on April 18. The proton fluxes are shown on a logarithmic scale with contours every decade.

[35] It should be pointed out that the proton precipitation patterns shown in Figures 7 and 8 do not completely characterize temporal variations, when compared to the solar wind drivers as shown in Figure 1. The large fluctuations observed in the solar wind density and IMF B_z during the sheath driven storm are not clearly demonstrated in the constructed patterns. This is because the 3-hour cadence selected in this study is larger than the time scale associated with these changes. The high-frequency temporal variations are therefore smoothed out and do not show up in the proton precipitation patterns. A similar limitation also applies to the patterns in the magnetic cloud driven storm. The sawtooth oscillations associated with energetic particle fluxes observed at geosynchronous orbit had a period of $2-3$ hours. It is hard to separate the intervals of enhanced particle injection from those of lower fluxes using a 3-hour time window. However, most of the precipitating high-energy protons are from the ring current, which usually exhibits changes on the order of several hours. That is, the magnetosphere acts as a low-pass filter between the solar wind and proton injection to the upper atmosphere. Therefore it is acceptable to use a 3-hour cadence for the pattern construction of energetic proton precipitation.

5.5. Quantification of Proton Precipitation Pattern Change

[36] So far this study has examined energetic proton precipitation on a global scale. It is of interest to extract quantities out of these patterns and compare to other measurements. The change of energetic proton precipitation patterns in the April 2002 storms is quantified in terms of three aspects: (1) hemispheric integrated total particle energy
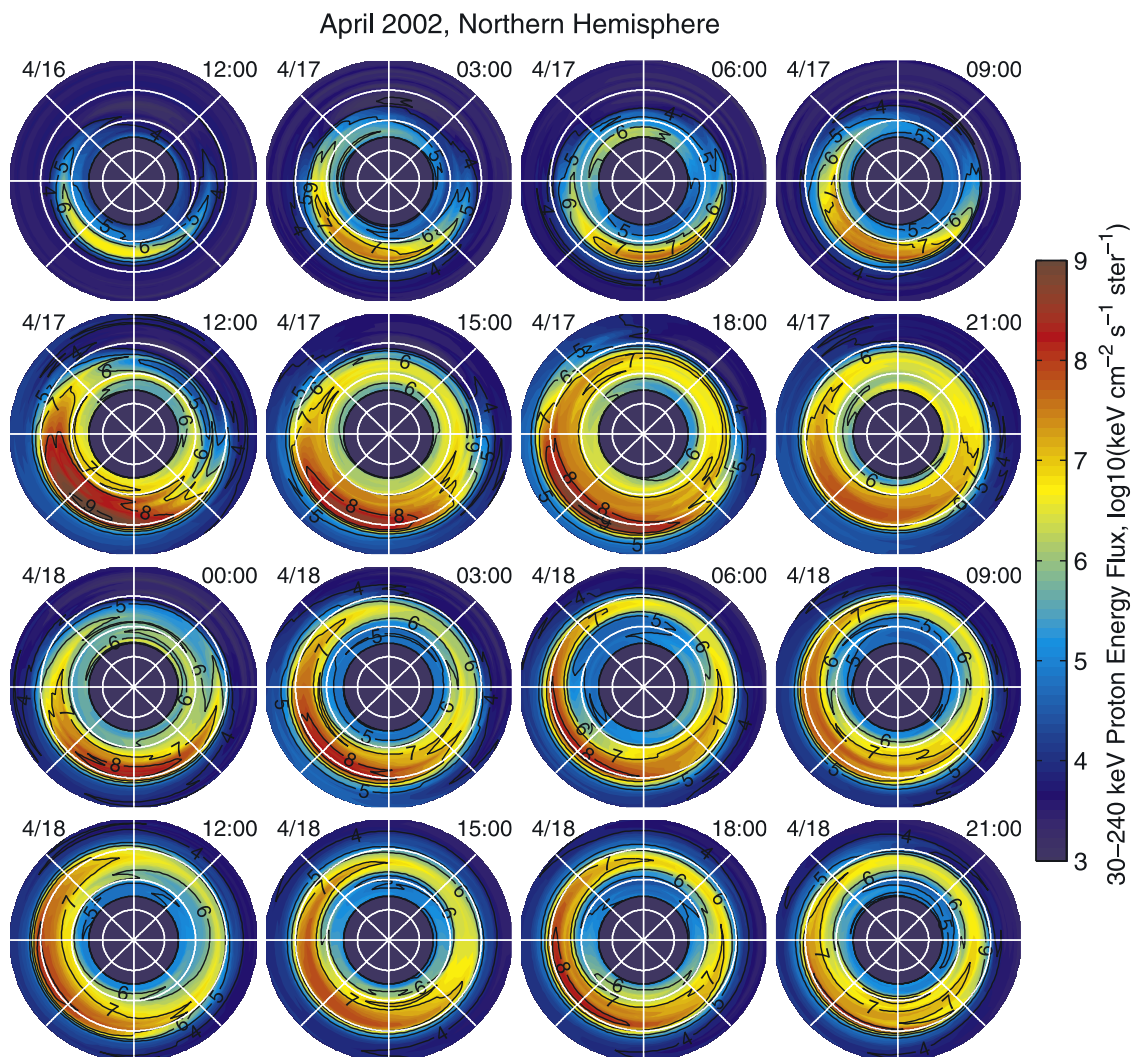
Figure 8. Similar to Figure 7, but for integrated energy fluxes. Note that in the chosen units, a value of 2×10^8 corresponds to 1 erg cm^{-2} s^{-1}.

influx, (2) midnight proton oval equatorward boundary, and (3) position of proton precipitation peak, as discussed in the following three subsections, respectively.

5.5.1. Hemispheric Total Energy Influx

[37] Figure 9 explores how energy flow into the auroral region in the northern hemisphere evolves with the storm development for different energy particles. Total NOAA/ POES 30–240 keV proton energy input integrated at a 3-hour cadence is compared against the hemispheric powers derived from the intersatellite adjusted precipitating electron and ion energies based on NOAA/TIROS and DMSP satellite measurements. The NOAA/TIROS low energy flux is carried by electrons and ions with the energy range of 300 eV–20 keV (SEM-1) or 50 eV–20 keV (SEM-2), while DMSP electron measurements cover the 30 eV–30 keV energy range. They have been intercalibrated and corrected for problems like sunlight contamination, noise, and sensor degradation, in the process of making the intersatellite adjusted hemispheric power. The details of this adjustment have been described by *Emery et al.* [2006].

[38] As shown in Figure 9, it is clear that the total precipitating energy of ions is generally one order of magnitude less than that of electrons during the storms. However, the relative energy contribution from high-energy ions (30–240 keV for NOAA/POES data) and low-energy ions (<20 keV for the NOAA SEM-2 intersatellite adjusted values) changed when the storms were triggered. Prior to the sheath arrival, most of the ion energy input was from <20 keV protons. However, as the storms developed, the scenario dramatically changed. The total precipitating energy from >30 keV ions was sharply enhanced by more than one order of magnitude, and became larger than or comparable to the low energy ion contribution. This feature remained present in the magnetic cloud driven storm on 18 April.

[39] Note that the percentage of total energy carried by 30–240 keV protons to that carried by 30–2500 keV protons had a mean of 95.3% with a standard deviation of 3.97%., as shown in Figure 10. It is thus safe to use 30–240 keV protons as a representative of total >30 keV proton energy input
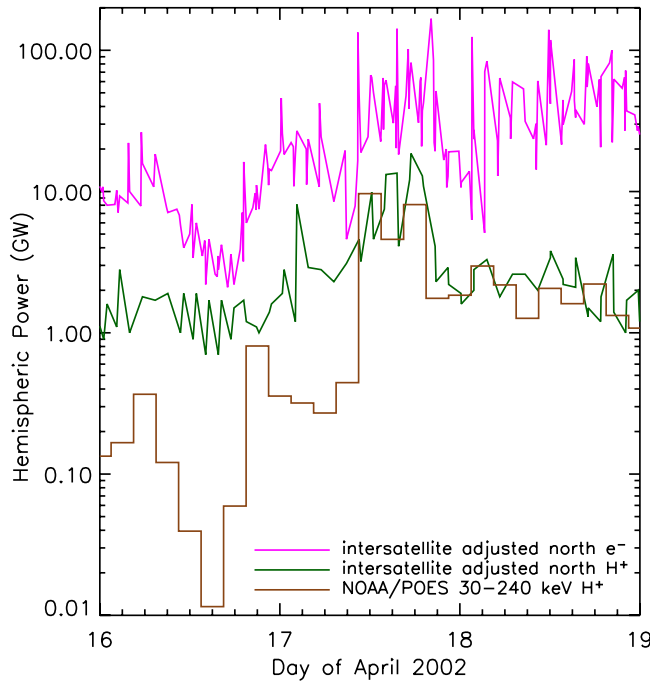
Figure 9. Northern hemispheric powers during 16–18 April 2002 derived from (magenta) intersatellite adjusted estimates of precipitating electron energy flux based on NOAA/TIROS <20 keV and DMSP <30 keV electron measurements, (green) estimated 50 eV to 20 keV ion energy flux from NOAA-15 and NOAA-16 SEM-2 intersatellite adjusted measurements, and (brown) estimated NOAA/POES 30–240 keV precipitating proton energy flux with a 3-hour cadence.

in the analysis of the 17–18 April 2002 storms. That is, Figures 7 and 8 actually represent global precipitation patterns of >30 keV protons.

5.5.2. Equatorward Edge at Midnight

[40] By analog with the ABI index [*Gussenhoven et al.*, 1983; *Madden and Gussenhoven*, 1990] for electron precipitation, an equatorward edge midnight boundary point can be defined for 30–240 keV protons (hereinafter referred to as ABI_{H^+}). To find ABI_{H^+}, the logarithmic values of midnight proton number flux at the equatorward slope are fitted using a Gaussian function, i.e.

$$g(\text{CML}) = p_0 + p_1 \exp\left(-\frac{(\text{CML} - \text{CML}_0)^2}{2\sigma^2}\right), \qquad (5)$$

where CML_0 is the peak location in corrected magnetic latitude, σ is the standard deviation, p_1 is the amplitude, and p_0 is a baseline adjustment. These four parameters are determined by least-square optimization. The ABI_{H^+} index is defined as $\sqrt{2}\sigma$ equatorward of the latitude of the fitted Gaussian curve peak, that is, $\text{CML}_0 - \sqrt{2}\sigma$.

[41] Figure 11 shows the positions of ABI_{H^+} in four examples as magnetospheric activity was quiet (16 April, 1200 UT), as the sheath struck the Earth (17 April, 1200 UT), as the magnetic cloud itself passed the Earth (18 April, 0000 UT), and in the global sawtooth oscillations (18 April,

0600 UT). It is shown that Gaussian curve fitting produces excellent agreement between observed and fitted data on the equatorward slope.

[42] The midnight energetic proton oval equatorward boundary has been identified for every 3-hour interval during the 16–18 April 2002 period, as illustrated in Figure 12 where the time evolution of ABI_{H^+} is compared against the other two indices: *Dst* (green curves) and ABI (blue curves). We can see that their time series followed almost the same overall trends. That is, as the storm developed with |*Dst*| increased (decreased), ABI and ABI_{H^+} moved equatorward (poleward). ABI_{H^+} was located equatorward of ABI, at most times within 1 degree of magnetic latitude. However, sometimes ABI_{H^+} and ABI can be apart by up to 4 degrees. For example, during the recovery phase of the sheath driven storm, electron precipitation (ABI) quickly returned back to high latitudes while >30 keV proton precipitation (ABI_{H^+}) slowly responded, leaving a latitude gap between them. This is because electrons have much faster decay time than ions. Keep in mind that these two quantities are different by definition. ABI is defined using <30 keV e^- measurement made by DMSP, while ABI_{H^+} is obtained by NOAA/POES 30–240 keV H^+ data. The low-latitude boundary of auroral electron precipitation is thought to mark ionospheric projection of the inner edge of the plasma sheet [*Kivelson*, 1976; *Southwood and Kaye*, 1979]. The observational strong correlation between ABI and ABI_{H^+} suggests that, in the midnight region, the equatorward edge of proton precipitation moves in the same way as the earthward approach of the near-Earth plasma sheet.

[43] It is useful to compare the ABI_{H^+} boundary against a similar value for lower energy ions. The IMAGE-FUV-SI12 instrument provides this alternative way to measure proton
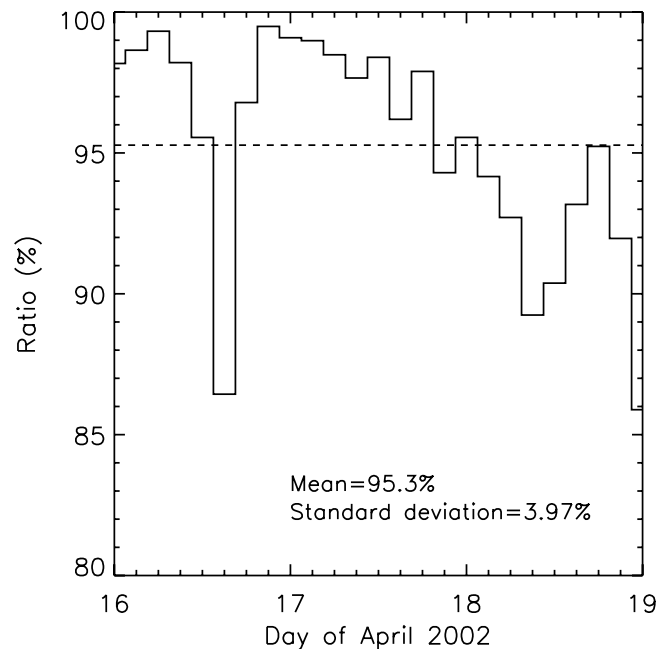
Figure 10. Percentage of hemispheric integrated energy input carried by 30–240 keV protons to that carried by 30–2500 keV protons during 16–18 April 2002. The dashed line indicates the average value.
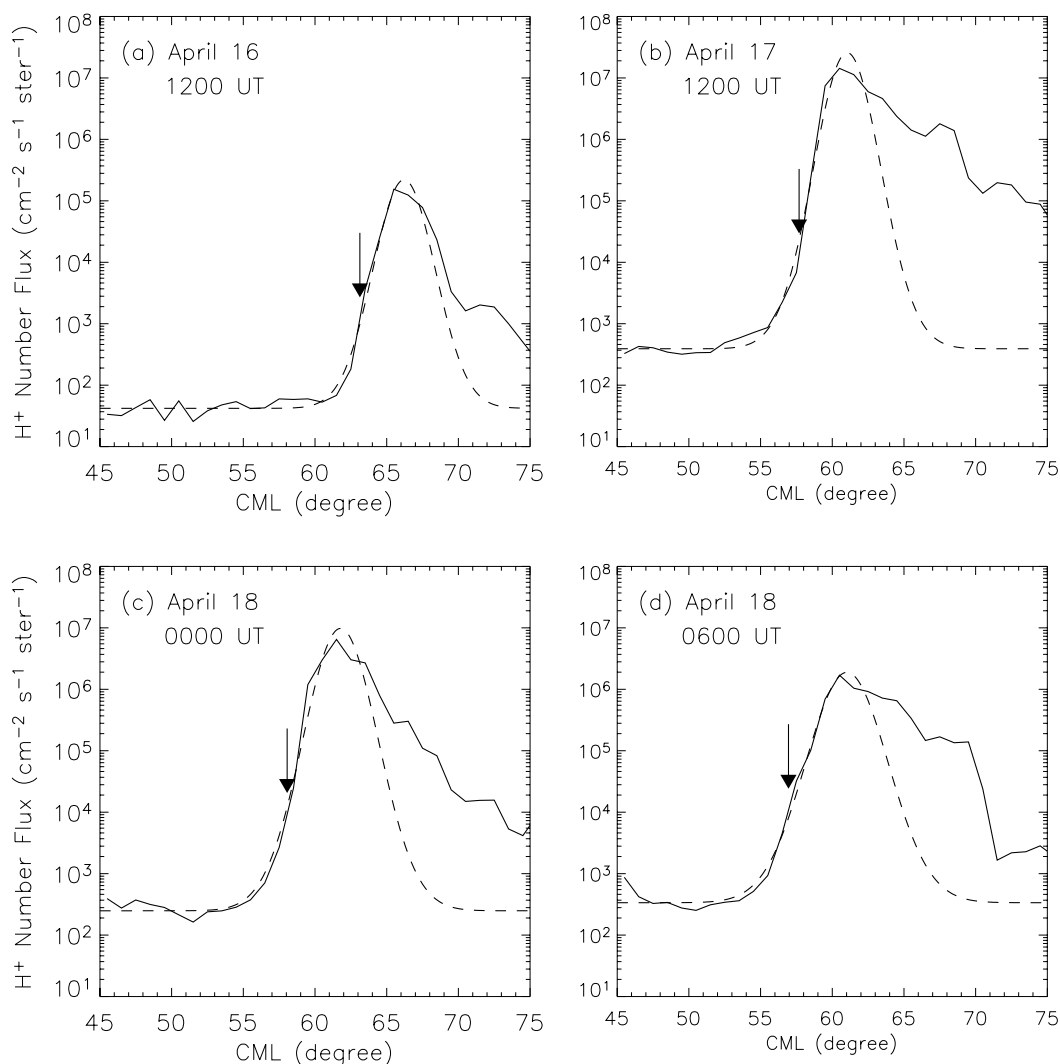
Figure 11. The 30–240 keV proton number flux at midnight (solid curves) versus magnetic latitude during a 3-hour interval centered at (a) 1200 UT on 16 April, (b) 1200 UT on 17 April, (c) 0000 UT on 18 April, and (d) 0600 UT on 18 April. The dashed curves are obtained by fitting the equatorward slopes of proton number flux with a Gaussian function. This is achieved by curve fitting on a logarithmic scale. The arrows mark the locations of ABI_{H^+}, the magnetic latitudes $\sqrt{2}\sigma$ equatorward of a fitted Gaussian curve peak (see text for details).

oval equatorward boundaries, focusing on medium energy particles. The SI12 [*Mende et al.*, 2000] is a grating-based instrument that is sensitive to emissions by >1 keV protons. The maximal sensitivity of SI12 is at 1218 $\mathring{A}$, which is emitted by downward moving hydrogen particles at energies of about 8 keV. Figure 13 presents an example of a snapshot of SI12 medium energy proton precipitation taken at 1500 UT on 17 April. Note that dayglow contamination was not removed on the dayside. The equatorward boundary of the nightside oval is estimated and superposed, under a similar process to that described by *DeJong and Clauer* [2005] for IMAGE-FUV-WIC images. The boundaries were first created automatically and then smoothed and manually adjusted for a better fit. This adjustment by hand can avoid a boundary accidentally shifting due to a stray bright pixel. A midnight equatorward boundary is thus calculated by

averaging the nearby boundaries within ±2.5° around 0000 MLT.

[44] The time series of the SI12 estimates of midnight equatorward boundaries has been overplotted in Figure 12, providing a comparison of >30 keV to medium energy proton precipitation. Note that the data have been averaged over 30 min. Data gaps occurred when the satellite was in the southern hemisphere. It is seen that >30 keV protons generally penetrated deeper (and thus lower magnetic latitudes) than the medium energy protons. This can be explained by the adiabatic energization of a convecting plasma sheet plasma. It should be pointed out that an exception took place during 1500–2100 UT on 17 April, in which the SI12 estimated midnight boundaries were located about 1 degree equatorward of ABI_{H^+}. However, this exception may not be physically meaningful, when
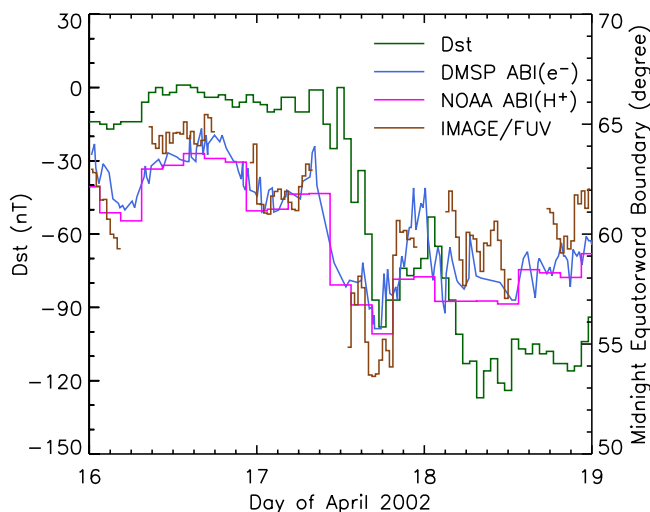
Figure 12. Comparison of ABI$_{H^+}$ against the *Dst* index on the left axis and two other midnight equatorward boundary positions on the right axis during 16–18 April 2002. ABI gives a midnight equatorward boundary estimation from DMSP electron measurements. The IMAGE-FUV-SI12 instrument provides an alternative way to measure the proton oval equatorward boundary with focus on medium energy particles.

examined closely and compared to another data set, that is, the DMSP 12–15 ion observations.

[45] During the time interval of 1500–2100 UT, the DMSP satellites passed through the geomagnetic dawn-dusk sector. The investigation at dawn and dusk showed that the NOAA/POES precipitating >30 keV proton boundaries were usually equatorward of the DMSP medium energy proton boundaries. Sometime in the interval, however, the two boundaries were located very close to each other. In addressing the unusual or unexpected midnight boundary locations during 1500-2100 UT on 17 April, several uncertainties must be considered. First, there was no local midnight coverage for the DMSP measurements. The in situ comparison was made in the dawn-dusk sector, and there is a lack of direct comparison at midnight. Second, NOAA/POES measurements were interpolated for a global coverage at 1-degree CML bins, which imposed a limitation on the latitudinal resolution. Third, different time scales were involved in the boundary extraction. NOAA/POES >30 keV proton precipitation patterns were generated in a 3-hour time interval, while IMAGE-FUV-SI12 medium energy proton oval observations had much higher time resolution (around 2 minutes) and were averaged over 30 min. Finally, an arbitrary emission intensity cutoff was used to extract SI12 nightside boundaries. The SI12 boundaries would be shifted poleward if using a higher threshold value. Therefore it is unclear whether it is useful to try to physically interpret the unusually low latitude for the <30 keV ion boundaries between 1500–2100 UT.

[46] To quantitatively investigate the relationship among the three indices (*Dst*, ABI, and ABI$_{H^+}$), a cross correlation analysis is performed and presented in Figure 14. To increase the number of data points for good statistics,

the time period covered was extended from 0300 UT on 14 April 2002 to 2100 UT on 26 April 2002 at a 3-hour cadence. That is, a total of 103 data points were incorporated into the cross correlation analysis. As shown in Figure 14, there is a remarkable positive correlation between the indices. It is worth noting that these correlation coefficients are so satisfactorily high that there is only a very tiny probability (<0.01%) of it occurring by chance. The high correlation among the three indices evident in Figure 14 suggests that the midnight proton oval equatorward boundary (ABI$_{H^+}$) is a good proxy of proton precipitation patterns, and thus a valuable tool for investigating the inner magnetospheric activity. The high correlation also implies that the usage of a 3-hour time window for the generation of the global energetic proton precipitation patterns is reasonable.

5.5.3. Position of Precipitation Peak

[47] Another way to quantify the proton pattern change is by observing the location of peak precipitation intensity in the storms. Figure 15 presents the time series of precipitation peak positions in CML and MLT during the 16–18 April 2002 storm events. It is seen that their motion demonstrated a significant correlation with respect to both *Dst* and ABI. In a general sense, as magnetospheric activity intensified, the peak precipitation location moved more westward away from midnight and more equatorward. This westward motion is qualitatively consistent with the westward drift observed for peak locations of the ring current pressure in recent statistical studies [*Lui*, 2003; *Le et al.*, 2004]. It is also consistent with the movement of the region 2 field aligned currents from data analysis [*Weimer*, 1999] and modeling [*Liemohn et al.*, 2001b].
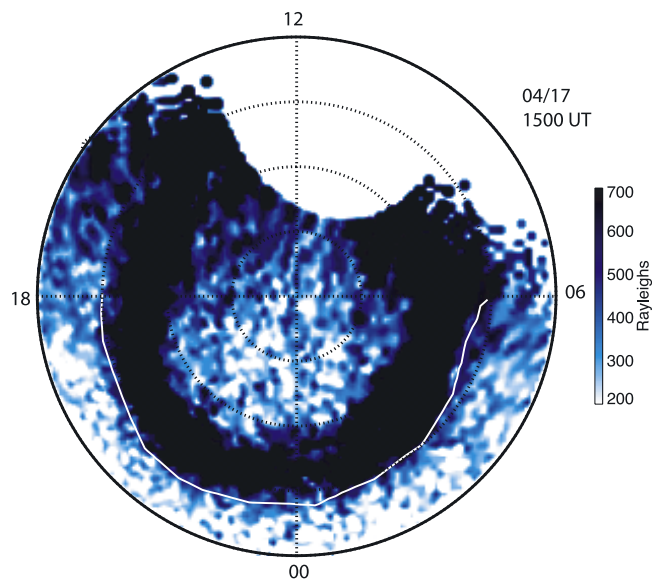
Figure 13. A snapshot of medium energy proton precipitation taken at 1500 UT on 17 April from the IMAGE-FUV-SI12 instrument. The solid curve is the nightside equatorward boundary at an intensity cutoff of 550 Rayleighs. The view is over the North Pole in CML-MLT coordinates with the Sun at the top. The perimeter latitude is 50° and the dotted circles are 10° apart.
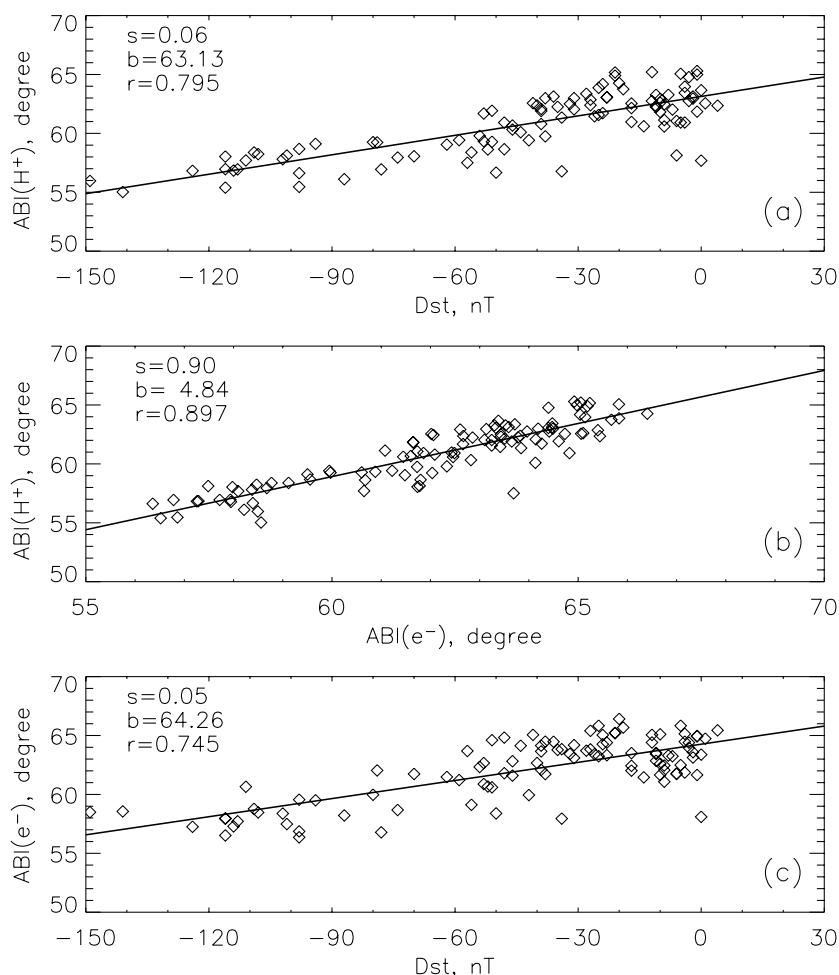
Figure 14. Scatter diagrams between (a) ABI_{H^+} and *Dst*, (b) ABI_{H^+} and ABI, and (c) ABI and *Dst*, at a 3-hour cadence from 0300 UT on 14 April 2002 to 2100 UT on 26 April. Linear regression lines are shown with the indicated slopes (*s*), intercepts (*b*), and correlation coefficients (*r*).

[48] Similar to Figure 14, a cross correlation analysis of the positions for 30–240 keV proton precipitation peak is summarized in Figure 16 against the *Dst* and ABI indices. This is performed during the time period of 0300 UT on 14 April to 2100 UT on 26 April with a 3-hour cadence. It is shown that the correlation for CML of precipitating H^+ number flux peak is systematically higher than that for the MLT values. While there is considerably more scatter for precipitation peak positions in MLT, a clear positive trend with the geomagnetic indices is illustrated in Figure 16. Note that all the correlation coefficients are still statistically significant at a probability level of <0.01%.

6. Summary and Conclusion

[49] Newly developed in situ 3-hour data products of the MEPED instruments onboard the NOAA/POES satellites have been used for the analysis of energetic proton precipitation patterns during the 17–18 April 2002 storm events. In situ measurements of the two NOAA/POES satellites at a 3-hour cadence is expected to have sufficient data points to construct a global morphology of proton ovals and have enough time resolution to investigate their dynamics as

well. April 2002 storm events are selected in this study, as they contain a rich spectrum of geophysical phenomena, including a sheath driven storm, a magnetic cloud driven storm, and global sawtooth oscillations. Without any specialized knowledge, the cosine fitting method to the MLT bin averaged data is selected in the study, as the 24-hour periodicity can be ensured and no special weight is given to any single MLT bin.

[50] There are several limitations on the method used in the construction of global proton precipitation patterns. First, NOAA-15 and NOAA-16 are the only NOAA/POES satellites operational during the selected April 2002 storms. The nature of the satellite orbits determines the limited spatial coverage associated with the data. Second, NOAA/POES ion measurements are collected in a 3-hour time window to construct global proton precipitation patterns. While this frequency is not sufficient to resolve rapid precipitation variations, it is the best cadence possible with NOAA's present fleet of satellites, and it is fast enough to resolve large-scale changes in the precipitation within each phase of a storm. Third, energetic (30–240 keV) proton precipitation is allowed for in this study, with the neglect of <30 keV plasma sheet ion injection. In a future study, this
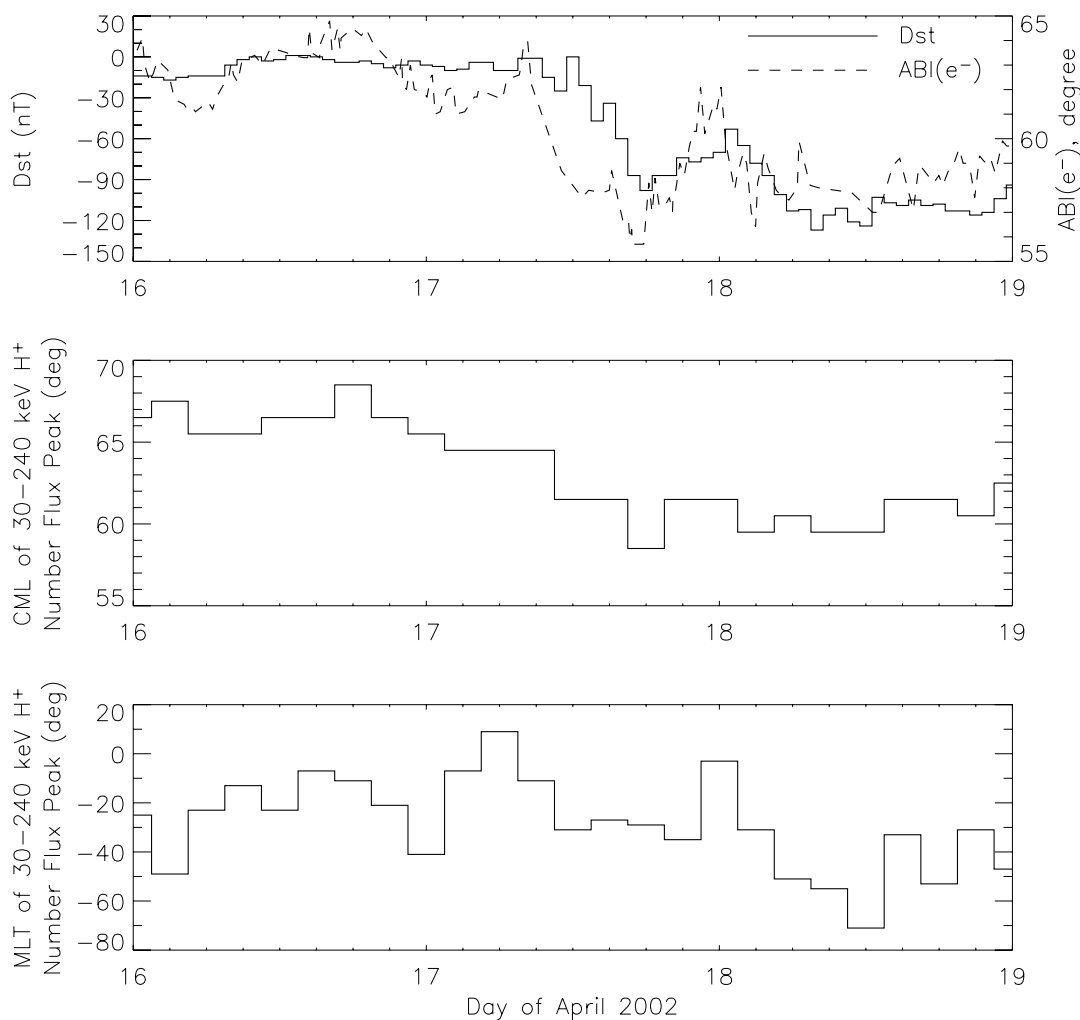
Figure 15. Locations of precipitating $30-240$ keV proton number flux peak during the time period of $16-18$ April 2002 at a 3-hour cadence: (middle) in magnetic latitude, and (bottom) in magnetic local time (measured in degree east of midnight). For comparison the time series of *Dst* and ABI indices are provided at the top.

lower energy part will be included to cover a full energy spectrum for proton precipitation. Fourth, without any specialized knowledge, a north-south symmetry assumption is made in this study. That is, to increase the density of data points, the measurements in the southern hemisphere are directly transferred to the northern hemisphere whenever there are no entries at magnetic conjugate points.

[51] The constructed 30-240 keV proton precipitation patterns have similar global morphologies for precipitating number and energy fluxes. The precipitation maps can be generally characterized by a C-shaped morphology with a roughly symmetric distribution about a meridian running premidnight to prenoon with a trough in the dawn-noon quadrant. The patterns during the sheath-driven storm (1107 UT on 17 April to 0000 UT on 18 April) and the magnetic cloud-driven storm (after 0000 UT on 18 April) clearly demonstrate notably distinct variability on a time-scale commensurate with the growth and decay of the plasma sheet and ring current. Because of largely fluctuating IMF B_z and high solar wind dynamic pressure, there was

more plasma sheet pressure buildup and thus higher auroral activity during the the sheath driven storm than during the magnetic cloud driven storm. In the global sawtooth oscillations associated with the magnetic cloud passage on 18 April, significant proton precipitation extended over all local times.

[52] The variation of energetic proton precipitation patterns has been quantified. Hemispheric total energy influx of $30-240$ keV protons is compared against intersatellite adjusted hemispheric powers carried by <20 keV electrons and ions (Emery et al., submitted manuscript, 2007). During the quiet time, >30 keV protons were a negligible energy source compared with lower-energy protons. However, as the storm was triggered by the solar wind high dynamic pressure at 1107 UT on 17 April, the energy flux carried by >30 keV protons was instantly enhanced by more than one order of magnitude and became larger than or comparable to the energy contribution from <20 keV ions. This remained present through the magnetic cloud driven storm on 18 April.
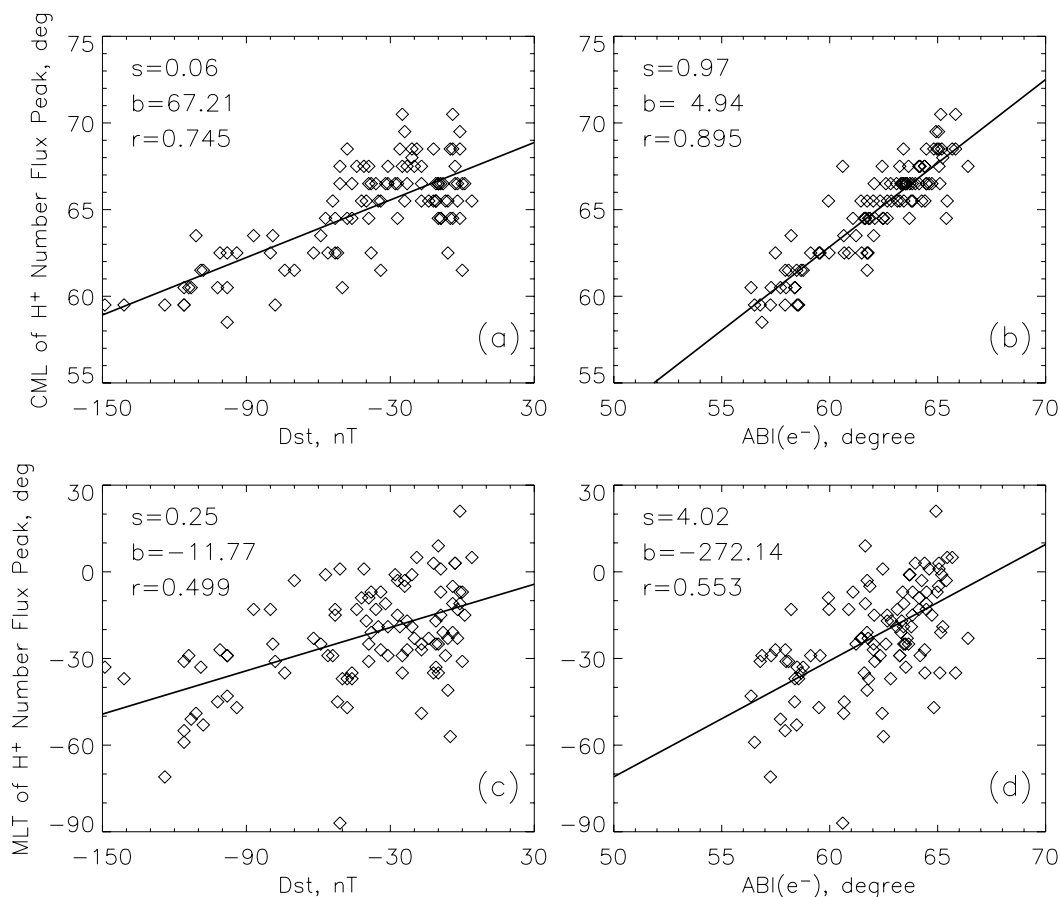
Figure 16. Similar to Figure 14 but for the scatter plots of (a) magnetic latitude of 30–240 keV proton precipitation peak versus *Dst*, (b) peak CML versus ABI, (c) peak MLT versus *Dst*, and (d) peak MLT versus ABI.

[53] By analog with the ABI index [*Gussenhoven et al.*, 1983; *Madden and Gussenhoven*, 1990] for electron precipitation, we derived a new index (ABI_{H^+}) for the midnight 30–240 keV proton oval equatorward boundary. A Gaussian function is used to fit the equatorward slope of precipitating proton number fluxes on a logarithmic scale. ABI_{H^+} is then defined as $\sqrt{2}\sigma$ equatorward of the fitted Gaussian curve peak. The time series of ABI_{H^+} during 16–18 April 2002 has been investigated and compared to the *Dst* and ABI indices as well as IMAGE-FUV-SI12 proton oval midnight equatorward boundaries. Their time series followed almost the same overall trends. In addition, the movement of the position of precipitating proton number flux peak in magnetic latitude and in magnetic local time was examined. It is found that as the storms developed, the midnight equatorward boundary tended to move to the lower latitude, while the precipitation peak moved equatorward and westward away from midnight. A cross correlation analysis was performed to investigate the relationship between the change of proton precipitation patterns and the geomagnetic index (*Dst* and ABI) development. The resulting cross correlation matrix is summarized in Table 2. For good statistics, the time period was extended to cover from 0300 UT on 14 April to 2100 UT on 26 April at a 3-hour cadence, with 103 data points included. The high statistical

correlation shows that 30–240 keV proton precipitation patterns can serve as a valuable diagnostic tool for investigating the inner magnetospheric activity. It also implies that the selection of a 3-hour time window for the creation of these global energetic proton precipitation maps is appropriate.

[54] The geoeffectiveness of global 30–240 keV proton precipitation during the April 2002 storms will be assessed in a companion paper by Fang et al. (manuscript in preparation). The constructed global ion precipitation patterns will be used as an energy input in a 3-D Monte Carlo ion transport model [*Fang et al.*, 2004, 2005]. The resulting ionization and heating rates to the atmosphere will then be

Table 2. Cross Correlation Coefficients Between 30 and 240 keV Proton Precipitation Patterns and Geomagnetic Indices During the Time Period of 0300 UT on 14 April to 2100 UT on 26 April at a 3-Hour Cadence

		Position of H⁺ Precipitation Peak	
	ABI_{H^+}	in CML	in MLT
Dst	0.795	0.745	0.499
ABI(e^-)	0.897	0.895	0.553

coupled with the Global Ionosphere-Thermosphere Model [*Ridley et al.*, 2004, 2006]. It will be the first time that the effect of protons on the dynamics in the thermosphere-ionosphere system will be presented and interpreted using observational global proton precipitation data instead of statistical patterns [*Galand et al.*, 1999, 2001].

References

Basu, B., J. R. Jasperse, D. J. Strickland, and R. E. Daniell Jr. (1993), Transport-theoretic model for the electron-proton-hydrogen atom aurora: 1. Theory, *J. Geophys. Res.*, *98*, 21,517.

Belian, R. D., G. R. Gisler, T. Cayton, and R. Christensen (1992), High-Z energetic particles at geosynchronous orbit during the great solar proton event series of October 1989, *J. Geophys. Res.*, *97*, 16,897.

Burch, J. L. (2000), IMAGE Mission overview, *Space Sci. Rev.*, *91*, 1.

Burch, J. L., et al. (2001), Views of Earth's magnetosphere with the IMAGE satellite, *Science*, *291*, 619.

Burton, R. K., R. L. McPherron, and C. T. Russell (1975), An empirical relationship between interplanetary conditions and *Dst*, *J. Geophys. Res.*, *80*, 4204.

Chua, D., G. Parks, M. Brittnacher, W. Peria, G. Germany, J. Spann, and C. Carlson (2001), Energy characteristics of auroral electron precipitation: A comparison of substorms and pressure pulse related auroral activity, *J. Geophys. Res.*, *106*, 5945.

Clauer, C. R., X. Cai, D. Welling, A. DeJong, and M. G. Henderson (2006), Characterizing the 18 April 2002 storm-time sawtooth events using ground magnetic data, *J. Geophys. Res.*, *111*, A04S90, doi:10.1029/2005JA011099.

Codrescu, M. V., T. J. Fuller-Rowell, R. G. Roble, and D. S. Evans (1997), Medium energy particle precipitation influences on the mesosphere and lower thermosphere, *J. Geophys. Res.*, *102*, 19,977.

Coumans, V., J.-C. Gérard, B. Hubert, S. B. Mende, and S. W. H. Cowley (2004), Morphology and seasonal variations of global auroral proton precipitation observed by IMAGE-FUV, *J. Geophys. Res.*, *109*, A12205, doi:10.1029/2003JA010348.

Davidson, G. T. (1965), Expected spatial distribution of low energy protons precipitated in the auroral zones, *J. Geophys. Res.*, *70*, 1061.

DeJong, A. D., and C. R. Clauer (2005), Polar UVI images to study steady magnetospheric convection events: Initial results, *Geophys. Res. Lett.*, *32*, L24101, doi:10.1029/2005GL024498.

Emery, B. A., D. S. Evans, M. S. Greer, E. Holeman, K. Kadinsky-Cade, F. J. Rich, and W. Xu (2006), The low energy auroral electron and ion hemispheric power after NOAA and DMSP intersatellite adjustments, *Sci. Tech. Rep. STR. 470*, Natl. Center for Atmos. Res., Boulder, Colo.

Evans, D. S., and M. S. Greer (2000), Polar Orbiting Environmental Satellite Space Environment Monitor 2: Instrument description and archive data documentation, *Tech. Memo. OAR SEC-93*, NOAA, Boulder, Colo.

Fang, X., M. W. Liemohn, J. U. Kozyra, and S. C. Solomon (2004), Quantification of the spreading effect of auroral proton precipitation, *J. Geophys. Res.*, *109*, A04309, doi:10.1029/2003JA010119.

Fang, X., M. W. Liemohn, J. U. Kozyra, and S. C. Solomon (2005), Study of the proton arc spreading effect on primary ionization rates, *J. Geophys. Res.*, *110*, A07302, doi:10.1029/2004JA010915.

Fok, M.-C., J. U. Kozyra, A. F. Nagy, C. E. Rasmussen, and G. V. Khazanov (1993), A decay model of equatorial ring current and the associated aeronomical consequences, *J. Geophys. Res.*, *98*, 19,381.

Frank, L. A., and J. D. Craven (1988), Imaging results from Dynamics Explorer 1, *Rev. Geophys.*, *26*, 249.

Galand, M., J. Lilensten, W. Kofman, and R. B. Sidge (1997), Proton transport model in the ionosphere: 1. Multistream approach of the transport equations, *J. Geophys. Res.*, *102*, 22,261.

Galand, M., R. G. Roble, and D. Lummerzheim (1999), Ionization by energetic protons in Thermosphere-Ionosphere Electrodynamics General Circulation Model, *J. Geophys. Res.*, *104*, 27,973.

Galand, M., T. J. Fuller-Rowell, and M. V. Codrescu (2001), Response of the upper atmosphere to auroral protons, *J. Geophys. Res.*, *106*, 127.

Gérard, J. C., B. Hubert, M. Meurant, V. I. Shematovich, D. V. Bisikalo, H. Frey, S. B. Mende, G. R. Gladstone, and C. W. Carlson (2001), Observation of the proton aurora with IMAGE FUV imager and simultaneous ion flux in situ measurements, *J. Geophys. Res.*, *106*, 28,939.

Gussenhoven, M. S., D. A. Hardy, and N. Heinemann (1983), Systematics of the equatorward diffuse auroral boundary, *J. Geophys. Res.*, *88*, 5692.

Hardy, D. A., M. S. Gussenhoven, and R. Raistrick (1987), Statistical and functional representations of the pattern of auoral energy flux, number flux, and conductivity, *J. Geophys. Res.*, *92*, 12,275.

Hardy, D. A., M. S. Gussenhoven, and D. Brautigam (1989), A statistical model of auroral ion precipitation, *J. Geophys. Res.*, *94*, 370.

Hardy, D. A., W. McNeil, M. S. Gussenhoven, and D. Brautigam (1991), A statistical model of auroral ion precipitation: 2. Functional representation of the average patterns, *J. Geophys. Res.*, *96*, 5539.

Henderson, M. G. (2004), The May 2–3, 1986 CDAW-9C interval: A sawtooth event, *Geophys. Res. Lett.*, *31*, L11804, doi:10.1029/2004GL019941.

Henderson, M. G., G. D. Reeves, R. Skoug, M. T. Thomsen, M. H. Denton, S. B. Mende, T. J. Immel, P. C. Brandt, and H. J. Singer (2006), Magnetospheric and auroral activity during the 18 April 2002 sawtooth event, *J. Geophys. Res.*, *111*, A01S90, doi:10.1029/2005JA011111.

Huang, C. S., J. C. Foster, G. D. Reeves, G. Le, H. U. Frey, C. J. Pollock, and J. M. Jahn (2003), Periodic magnetospheric substorms: Multiple space-based and ground-based instrumental observations, *J. Geophys. Res.*, *108*(A11), 1411, doi:10.1029/2003JA009992.

Huang, C. S., G. D. Reeves, G. Le, and K. Yumoto (2005), Are sawtooth oscillations of energetic plasma particle fluxes caused by periodic substorms or driven by solar wind pressure enhancements?, *J. Geophys. Res.*, *110*, A07207, doi:10.1029/2005JA011018.

Hubert, B., J.-C. Gérard, D. V. Bisikalo, V. I. Shematovich, and S. C. Solomon (2001), The role of proton precipitation in the excitation of auroral FUV emissions, *J. Geophys. Res.*, *106*, 21,475.

Hubert, B., J.-C. Gérard, S. A. Fuselier, S. B. Mende, and J. L. Burch (2004), Proton precipitation during transpolar auroral events: Observations with the IMAGE-FUV imagers, *J. Geophys. Res.*, *109*, A06204, doi:10.1029/2003JA010136.

Jasperse, J. R., and B. Basu (1982), Transport-theoretic solutions for auroral proton and H atom fluxes and related quantities, *J. Geophys. Res.*, *87*, 811.

Jordanova, V. K., L. M. Kistler, J. U. Kozyra, G. V. Khazanov, and A. F. Nagy (1996), Collisional losses of ring current ions, *J. Geophys. Res.*, *101*, 111.

Kivelson, M. G. (1976), Magnetospheric electric fields and their variations with geomagnetic activity, *Rev. Geophys.*, *14*, 189.

Kozelov, B. V. (1993), Influence of the dipolar magnetic field on transport of proton-H atom fluxes in the atmosphere, *Ann. Geophys.*, *11*, 697.

Le, G., C. T. Russell, and K. Takahashi (2004), Morphology of the ring current derived from magnetic field observations, *Ann. Geophys.*, *22*, 1267.

Lee, D. Y., L. R. Lyons, and K. Yumoto (2004), Sawtooth oscillations directly driven by solar wind dynamic pressure enhancements, *J. Geophys. Res.*, *109*, A04202, doi:10.1029/2003JA010246.

Liemohn, M. W., J. U. Kozyra, V. K. Jordanova, G. V. Khazanov, M. F. Thomsen, and T. E. Cayton (1999), Analysis of early phase ring current recovery mechanisms during geomagnetic storms, *Geophys. Res. Lett.*, *25*, 2845.

Liemohn, M. W., J. U. Kozyra, M. F. Thomsen, J. L. Roeder, G. Lu, J. E. Borovsky, and T. E. Cayton (2001a), Dominant role of the asymmetric ring current in producing the stormtime *Dst**?, *J. Geophys. Res.*, *106*, 10,883.

Liemohn, M. W., J. U. Kozyra, C. R. Clauer, and A. J. Ridley (2001b), Computational analysis of the near-Earth magnetospheric current system during two-phase decay storms, *J. Geophys. Res.*, *106*, 29,531.

Liemohn, M. W., A. J. Ridley, D. L. Gallagher, D. M. Ober, and J. U. Kozyra (2004), Dependence of plasmaspheric morphology on the electric field description during the recovery phase of the 17 April 2002 magnetic storm, *J. Geophys. Res.*, *109*, A03209, doi:10.1029/2003JA010304.

Liemohn, M. W., J. U. Kozyra, A. J. Ridley, M. F. Thomsen, M. G. Henderson, P. C. Brandt, and D. G. Mitchell (2007), Modeling the ring current response to a sawtooth oscillation event, *J. Atmos. Sol. Terr. Phys.*, *69*, 67.

Lui, A. T. Y. (2003), Inner magnetospheric plasma pressure distribution and its local time asymmetry, *Geophys. Res. Lett.*, *30*(16), 1846, doi:10.1029/2003GL017596.

Lui, A. T. Y., T. Hori, S. Ohtani, Y. Zhang, X. Y. Zhou, M. G. Henderson, T. Mukai, H. Hayakawa, and S. B. Mende (2004), Magnetotail behavior during storm time ''sawtooth injections'', *J. Geophys. Res.*, *109*, A10215, doi:10.1029/2004JA010543.

Lyons, L. R. (2000), Geomagnetic disturbances: characteristics of, distinction between types, and relations to interplanetary conditions, *J. Atmos. Sol. Terr. Phys.*, *62*, 1087.

Madden, D., and M. S. Gussenhoven (1990), Auroral Boundary Index from 1983 to 1990, *Tech. Rep. GL-TR-90-0358*, Air Force Geophys. Lab., Hanscom Air Force Base, Mass.

McComas, D. J., S. J. Bame, P. Baker, W. C. Feldman, J. L. Philips, and P. Riley (1998), Solar wind electron proton alphamonitor (SWEPAM) for the Advanced Composition Explorer, *Space Sci. Rev.*, *86*, 563.

Mende, S. B., et al. (2000), Far ultraviolet imaging from the IMAGE spacecraft, 3, Spectral imaging of Lyman-alpha and OI 135.6 nm, *Space Sci. Rev.*, *91*, 287.

Mende, S. B., H. U. Frey, T. J. Immel, D. G. Mitchell, P. C:son-Brandt, and J.-C. Gérard (2002), Global comparison of magnetospheric ion fluxes and auroral precipitation during a substorm, *Geophys. Res. Lett.*, *29*(12), 1609, doi:10.1029/2001GL014143.

Raben, V. J., D. E. Evans, H. H. Sauer, S. R. Sahm, and M. Huynh (1995), TIROS/NOAA satellite space environment monitor data archive documentation: 1995 update, *Tech. Memo. ERL SEC-86*, Natl. Oceanic and Atmos. Admin., Boulder, Colo.

Reeves, G. D., et al. (2002), Global ''Sawtooth'' activity in the April 2002 geomagnetic storm, *Eos Trans. AGU*, *83*(47), Fall Meet. Suppl., Abstract SA12A-05.

Reeves, G. D., et al. (2003), IMAGE, POLAR, and geosynchronous observations of substorm and ring current ion injection, in *Disturbances in Geospace: The Storm-Substorm Relationship*, *Geophys Monogr. Ser.*, vol. 142, edited by A. S. Sharma, Y. Kamide, and G. S. Lakhina, pp. 89–100, AGU, Washington, D. C.

Reiff, P. H., R. W. Spiro, and T. W. Hill (1981), Dependence of polar cap potential drop of interplanetary parameters, *J. Geophys. Res.*, *86*, 7639.

Ridley, A. J., G. Tóth, Y. Deng, J. Kozyra, T. Immel, and L. Paxton (2004), The Global Ionosphere Thermosphere Model results of the April 2002 storm, *Eos Trans. American Geophysical Union*, *85*(17), Jt. Assem. Suppl., Abstract SA41A-07.

Ridley, A. J., Y. Deng, and G. Tóth (2006), The global ionosphere-thermosphere model, *J. Atmos. Sol. Terr. Phys.*, *68*, 839.

Siscoe, G. L., G. M. Erickson, B. U. Ö. Sonnerup, N. C. Maynard, J. A. Schoendorf, K. D. Siebert, D. R. Weimer, W. W. White, and G. R. Wilson (2002), Hill model of transpolar potential saturation: Comparisons with MHD simulations, *J. Geophys. Res.*, *107*(A6), 1075, doi:10.1029/2001JA000109.

Smith, C. W., M. H. Acuna, L. F. Burlaga, J. L. Heureux, N. F. Ness, and J. Scheifele (1998), The ACE magnetic field experiment, *Space Sci. Rev.*, *86*, 613.

Solomon, S. C. (2001), Auroral particle transport using Monte Carlo and hybrid methods, *J. Geophys. Res.*, *106*, 107.

Southwood, D. J., and S. M. Kaye (1979), Drift boundary approximations in simple magnetospheric convection models, *J. Geophys. Res.*, *84*, 5773.

Torr, M. R., et al. (1995), A far ultraviolet imager for the international solar-terrestrial physics mission, in *The Global Geospace Mission*, edited by C. Russell, p. 329, CED-Samson/Wolters Kluwer, Diegem, Belgium.

Weimer, D. R. (1999), Substorm influence on the ionospheric electric potentials and currents, *J. Geophys. Res.*, *104*, 185.

————————————

A. D. DeJong, X. Fang, J. U. Kozyra, and M. W. Liemohn, Space Physics Research Laboratory, University of Michigan, 2455 Hayward Street, Ann Arbor, MI 48109-2143, USA. (dejonga@umich.edu; xhfang@umich.edu; jukozyra@umich.edu; liemohn@umich.edu)

B. A. Emery, High Altitude Observatory, National Center for Atmospheric Research, Boulder, CO 80307, USA. (emery@ucar.edu)

D. S. Evans, Space Environment Center, NOAA, 325 Broadway, Boulder, CO 80303, USA. (david.s.evans@noaa.gov)